PHILOSOPHICAL TRANSACTIONS OF THE ROYAL SOCIETY A MATHEMATICAL, PHYSICAL & ENGINEERING SCIENCES

Electronic Properties of Well Oriented Graphite

I. L. Spain, A. R. Ubbelohde and D. A. Young

Phil. Trans. R. Soc. Lond. A 1967 **262**, 345-386
doi: 10.1098/rsta.1967.0053

ELECTRONIC PROPERTIES OF WELL ORIENTED GRAPHITE

By I. L. Spain, A. R. Ubbelohde, F.R.S., and D. A. Young

Department of Chemical Engineering and Chemical Technology, Imperial College, London, S.W. 7

(*Received* 7 *February* 1966—*Revised* 23 *December* 1966)

[Plate 6]

CONTENTS

A range of dense well oriented graphites of high chemical purity has been prepared by stress recrystallization of pyrolytic material. Systematic trends in the galvanomagnetic and thermoelectric properties have been investigated in relation to *c*-axis distribution function, crystallite size, and basal plane dislocation concentration, using temperatures from 300 to 1·2 °K and magnetic fields up to 6700 G. Basal plane properties of ideal graphite are evaluated in terms of the trends observed.

Electronic properties have been measured parallel to the *c* axis for corresponding graphites with a range of defect concentrations. From the trends established, estimates are made of various properties of ideal defect-free graphite in the *c*-axis direction, and of anisotropy ratios. Effects of neutron irradiation on some of the electronic properties are also described. Results are discussed in terms of multi-carrier models.

Vol. 262. A. 1128. (Price 16*s*. 6*d*.; U.S. $2.45) 44 [Published 6 October 1967

Introduction

Studies of physical, and in particular of electronic, properties of crystallographically ideal graphite are hampered by the scarcity of natural single crystals of moderate size that are free from gross defects and inorganic inclusions. If not removed, such inclusions may cause lattice distortions and may inject or abstract electrons from the band system. Since the number of charge carriers is only of the order 10^{-4} per atom, the electronic properties of graphite are sensitive even to small charge transfers by impurities and intercalates. Even if impurities are carefully removed by chemical treatment (see, for example, Soule 1958, specimen EP 14), resulting scars in the crystals, which may, for example, be regions of rhombohedral stacking between twin walls, are difficult to eliminate with complete certainty; yet they may have a profound effect on the band structure. Isolated studies on natural single crystals, however well selected and carefully handled, thus cannot establish definitive values for *ideal* graphite. A more systematic approach to this problem by the study of trends in a range of recrystallized graphites of high chemical purity was therefore adopted. Data on 'good' natural single crystals can then be fitted into this range, and provide useful approximations to the ideal norm.

Earlier exploratory investigations (Blackman, Saunders & Ubbelohde 1961) covered a wide range of pyrolytic carbons. The present series of experiments refers to a much narrower range of recrystallized graphites, selected for their asymptotic approach to the resistivity of an ideal single crystal.

As starting materials, the graphites were prepared by pyrolysis of methane, and contained only hydrogen as residual impurity; in selected materials concentrations were below analytically detectable values ($H < 10^{-5}$ atom per atom). Despite densities not far from the crystallographic limit (2·2654 g/cm^3; Wyckoff 1960) even the best of such materials have much less perfect texture than the best natural crystals. Greatly improved texture was achieved by hot pressing pyrolytic deposits (Ubbelohde, Young & Moore 1963) yielding specimens in which the crystallites have their c-axes accurately alined, with basal plane crystallite dimensions up to 2·5 μm.

This paper first deals with measurements of electrical transport properties in the basal plane. When the data are examined in terms of a multi-carrier model, marked divergencies from some aspects of the behaviour of natural crystals are apparent. These investigations permitted reliable evaluation of basal plane electronic properties in relation to preparative procedure, and established estimates of the properties of ideal defect-free graphite, regarded as an asymptotic limit. Production by hot-pressing and annealing yields uniform specimens thick in the direction of the c axis, and thus also facilitates direct experimental measurements of conduction properties normal to the basal plane. Previous attempts to investigate c-axis properties have employed either procedures ingeniously adapted to thin specimens, or have involved thicker materials that were but poorly characterized. The broad c-axis distribution function that often applies to such unsatisfactory materials encompasses effects of enhanced resistivity due to voids, reduced resistivity due to a-axis contributions from maloriented crystallites, and uncertain contributions from intergranular resistance. Use in the present work of the same range of tested materials for both directions permitted much more reliable characterization. As it happened a number of

c-axis electronic properties proved to be considerably less sensitive to the presence of imperfections than their basal plane counterparts. Apparently limiting values independent of the defect content are attained at relatively high concentrations of residual imperfections. This gave further support to the view that such *c*-axis properties are characteristic for ideal defect-free graphite, and are thus of definitive significance for theoretical work.

Experimental

Details of fabrication of dense, well oriented graphites by hot-pressing and stress-recrystallization have been previously published (Moore *et al.* 1964). Materials so obtained, normally cylinders of height ($\parallel c$ axis) 1 to 2 cm and diameter ($\perp c$ axis) 1·25 cm could readily be cleaved to expose mirrorlike basal plane surfaces (Spain, Ubbelohde & Young (1965)).

Characterization of the samples

As lattice imperfections of all kinds are successively eliminated, the physical properties of the materials used in the present work approach limiting values in characteristic ways. Before selecting the most suitable properties for establishing asymptotes to ideal behaviour, a wide range was studied. In the sequence of materials used, the preparative conditions were made progressively more stringent.

General physical properties

Density. In the work described below, only one of the hot-pressed samples had a density lower than 2·257 g/cm^3 (void volume $< 0{\cdot}4\%$) and most of them had a density not lower than 2·263 g/cm^3 (void volume $< 0{\cdot}1\%$ on a theoretical density 2·2654 g/cm^3) measured by weighing in air and water with an accuracy of $\pm 0{\cdot}001$ g/cm^3.

Thermal conductivity. Above 300 °K thermal resistance in the basal plane arises predominantly from Umklapp processes and is thus intrinsic. It appears to be sensitive to phonon scattering by dislocations in the temperature range 150 to 300 °K, a process which is replaced in importance by boundary scattering as the temperature is lowered still further (Hooker, Ubbelohde & Young 1963, 1965*a*, *b*). Thus the thermal resistance is a useful guide to the imperfection content. At intermediate temperatures the information obtained was only qualitative, but in logarithmic plots of thermal conductivity against temperature, the low temperature asymptote to the T^2 specific heat slope gave a quantitative measure of the basal-plane dimensions of the crystallites.

X-ray diffraction

Three procedures were used for testing:

(*a*) *Non-destructive topological examination of large specimens*

A beam of X-rays (Mo$K\alpha$, filtered) was passed normal to the cylinder axis of hot pressed specimens, held stationary. The photographic plate was mounted perpendicular to the incident beam 4 cm away. This should yield a single crystal *c*-axis rotation photograph, with reflexions (*h*0*l*) (*h*1*l*), etc., elongated along the radial direction. Provided these elongations were straight, the (002) reflexions were weak, and the (004) and higher order reflexions absent, it was concluded that the sample was well oriented, and that the basal

planes were not wrinkled by cone structures not completely removed by hot-pressing. Unacceptable samples contained long-wavelength (1 to 3 mm) wrinkles in the basal planes, with the elongated reflexions jagged and the (00*l*) reflexions of low order strengthened. Figure 1*a*, *b*, plate 6, illustrates comparative diffraction photographs of a good and a less perfect texture obtained as described. Figure 1*c* is a corresponding diffraction photograph of a good quality graphite taken on a 6 cm diameter cylindrical film. (Thanks are due to Dr D. Nixon for this photograph.)

(*b*) *Diffractometer examination*

In a cleaved sheet (e.g. 0·5 mm thick), crystallite misorientation was determined on an uncoupled diffractometer, a filtered microbeam and conventional procedures being used.

The findings can be represented either as the complete *c*-axis distribution function at a given position in the sample, or as the width of the distribution of *c* axes as a function of position of the diffracting volume within the sample (cf. Moore *et al.* 1964). The present work deals mainly with materials for which the *full width at half maximum* lies within 0·4°. Occasionally materials were used for which the full width lies within 1°.

Procedure (*b*), unlike (*a*), gave no information about long wavelength ripples in the basal planes. This was unfortunate because these ripples, which are difficult to eliminate or quantify, exert a powerful effect on the anisotropy of the magnetoresistance (see below).

(*c*) *Microfocus X-ray examination*

Specimens for the present experiments could readily be cleaved to give flakes 10 to 20 μm thick. In Laue photographs of such flakes taken a with 30 μm X-ray beam parallel to the *c* axis (Parry & Young, unpublished observations) the diffuse rings were broken up to form radial streaks, consistent with basal plane crystallite dimensions of 1 to 1·5 μm. Stacking faults involving rotation of one good crystallite through about 1° with respect to its neighbour were common, as was also confirmed by electron diffraction. Method (*c*) served to detect recrystallized soot nuclei which had survived basal shear during preparation, and in which the orientations departed radically from their environment (Moore *et al.* 1964). Samples retaining nuclei of this kind were rejected except in three cases (SA 11, 13, 22). Despite the inclusion of soot particles, it may be noted that the angular *c*-axis distribution of sample SA 22 is very narrow.

Electron microscopy and diffraction

Techniques were used to detect (and in most cases to reject) material containing lenticular voids or soot nuclei (figure 1*d*, plate 6). In the best graphites the content of dislocations (figure 1*e*) revealed by these techniques was less than 10^4 cm/cm^2, of projected area, with a basal plane diameter L_a for single crystal domains ranging between 2 and 5 μm. Preliminary evidence suggested that $L_c \approx 1000$ to 2000 Å; normally the *c*-axis boundary marked rotation of neighbouring crystallites through an angle of the order of 1° about the *c* axis.

Design of sample geometry

For materials of present interest the electrical anisotropy might rise as high as 10^4 (Blackman *et al.* 1961). In view of this exceptionally high anisotropy, to obtain valid

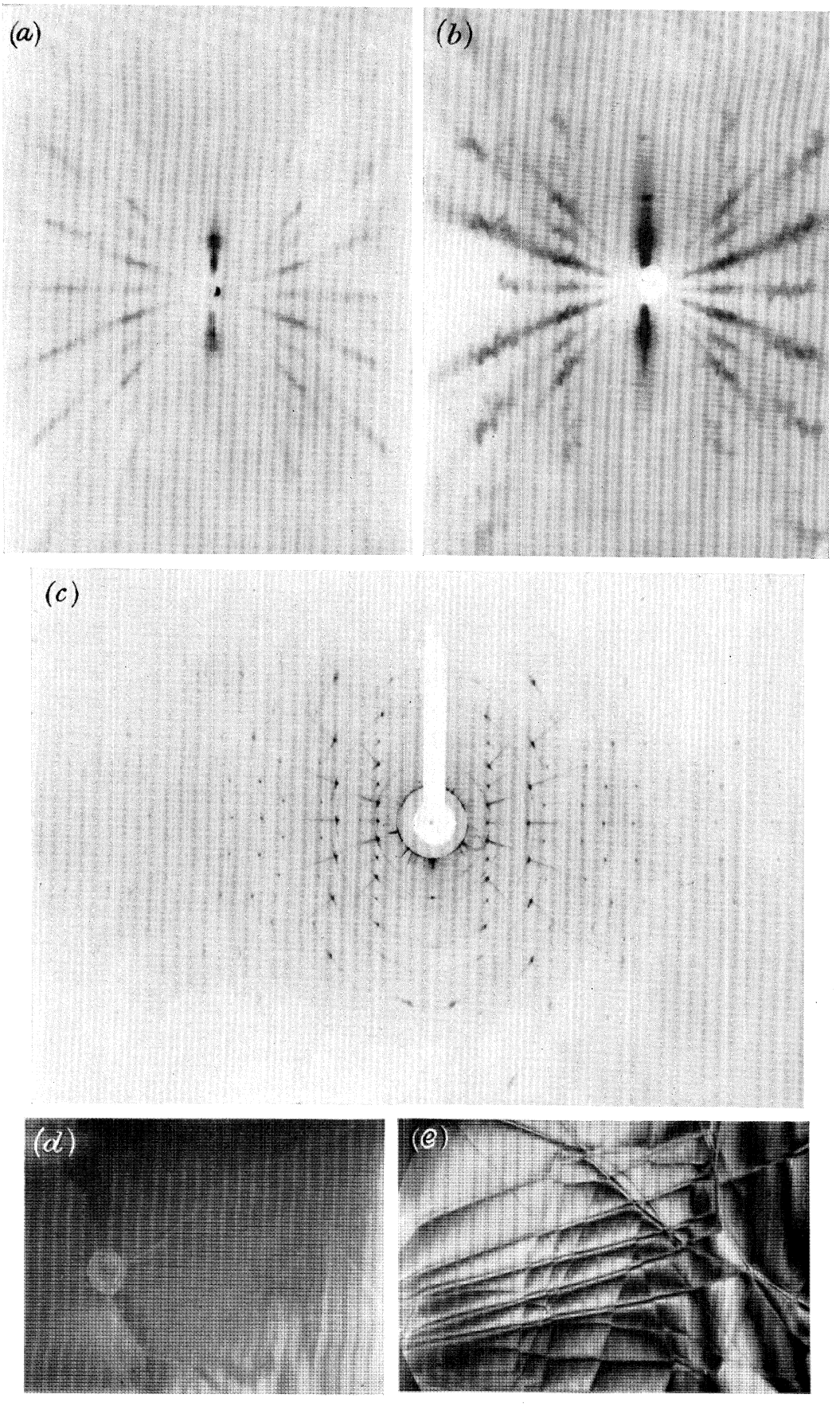

FIGURE 1. (*a*) X-ray photograph of flat disk (IFP 53) taken with Mo$K\alpha$ beam parallel to basal planes. Note isostatic zone at the edge of the disk. (Moore *et al.* 1964; Spain *et al.* 1965). (*b*) As above, but for a rippled cleavage surface (Sample IFP 1). (*c*) X-ray diffraction pattern (Mo$K\alpha$) of sample SA 26 (JHP 1) taken on a cylindrical film. Note $\alpha_1\alpha_2$ splitting. (*d*) Electron micrograph of a soot nucleus (magn. $\times 6500$) (IFP 37) (Moore *et al.* 1964). (*e*) Basal dislocation network in annealed material (magn. $\times 6500$) (IFP 37).

(*Facing p.* 348)

PHILOSOPHICAL TRANSACTIONS OF THE ROYAL SOCIETY A MATHEMATICAL, PHYSICAL & ENGINEERING SCIENCES

measurements a prime need was to ensure that each basal plane carried an equivalent current, that isopotential lines were parallel and straight between the voltage probes, and that the presence of the voltage probes did not affect the current distribution.

The hexagonal symmetry D_{6h} of each individual crystallite may for many purposes be replaced by the approximately cylindrical symmetry of the macroscopic sample. To this approximation, three geometries are of importance, as illustrated in figure 2*a*, *b*, *c*.

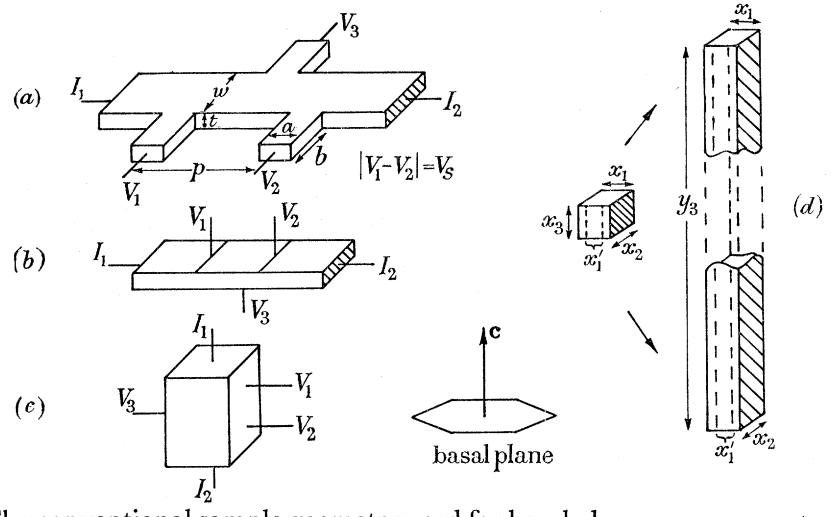

FIGURE 2. (*a*) The conventional sample geometry used for basal plane measurements. (*b*) A configuration which was difficult to fabricate, and not used. (*c*) This configuration was used for *c*-axis measurements. (*d*) The linear transformation to an isotropic analogue.

In practice, configuration 2*a*, which is conventional, proved simple to fabricate. Methods developed for configuration 2*c* required for *c*-axis measurements are described below. Configuration 2*b* proved to be extremely difficult to fabricate in a satisfactory way. Since not more than two configurations are required for the complete determination of the magneto-conductivity tensor for cylindrical symmetry $\sigma_{ij}(H) = \sigma_{ji}(-H)$, attention was concentrated on configurations 2*a* and 2*c*.†

Analogue experiments to determine current distributions were carried out on conducting paper (Olsen 1962) assuming $\rho_c/\rho_a = 10^4$; subsequently it was found that this ratio can rise to $8{\cdot}86 \times 10^4$ at 4·2 °K; but this does not seriously affect procedures described below.

An anisotropic solid with principal conductivities σ_1, σ_2, σ_3, along principal axes x_1, x_2, x_3, can be referred to axes y_1, y_2, y_3 in an isotropic solid with conductivity $\sigma = (\sigma_1\sigma_2\sigma_3)^{\frac{1}{3}}$ according to the transformation (cf. Nye 1957)

$$x_i = \sigma^{-\frac{1}{2}}\sigma_i^{\frac{1}{2}}y_i \quad (i = 1, 2, 3).$$

The rotational symmetry of hot pressed graphite requires $\sigma_1 = \sigma_2 \neq \sigma_3$ where $x_3 \| y_3 \| \mathbf{c}$, in which case a cubic block of graphite would transform to a column of isotropic material of square cross-section with

$$y_3/y_1 = y_3/y_2 = (\sigma_1/\sigma_3)^{\frac{1}{2}},$$

i.e.

$$y_3 = 100y_1 = 100y_2.$$

† 2*a* gives $\sigma_{xx} = \sigma_{yy}$ and σ_{xy}; 2*c* would give σ_{zz} and $\sigma_{zx} = \sigma_{zy}$ and 2*b* would give $\sigma_{xx} = \sigma_{yy}$ and $\sigma_{zx} = \sigma_{zy}$.

Accordingly, the problem is to establish constant (preferably negligible), contact resistance over the shaded and end-surfaces of a material which if isotropic would have the shape shown in the sketch (figure 2*d*).

In practice, it was a simple matter to make x_3 about 0·03 to 0·06 cm, the dimension x_1 being fixed at about 1 cm by the size of the preparation. For Hall effect measurements to be meaningful the width $x_2 \leqslant x_1/5$. For all measurements x_2 was made about 0·15 to 0·2 cm. The distance between potential probes was in the range 0·25 to 0·5 cm. For such a sample, with a length/thickness ratio of about 20, the isotropic analogue is only 5 times as broad as it is long. Even so, care must be taken to eliminate fluctuations in contact resistance over the current electrode surfaces.

Examination of the disturbance of the current flow by the introduction of potential probes, with b/a between 1 and 2, showed that for typical values of a/p (cf. figure 2*a* for symbols) the correction to be applied to the formula for the resistivity

$$\rho = \frac{V_s}{j}\frac{wt}{p}$$

is less than 0·2 %. This is negligible compared with uncertainties in the measurements of the dimensions w, t and p.

Analogue experiments and sample conformation do not give problems in the same form when the current is in the c-axis direction. For this case, the isotropic analogue is long and thin, and the main difficulty is that current may flow in the copper contacts of the voltage probes, short-circuiting the main current. Two sample geometries indicated by analogue experiments on conducting paper were adopted. Figure 3*a* illustrates a conventional design, which employed tapered potential probes to reduce the short-circuiting by the plated copper. Figure 3*b* illustrates a geometry in which the copper for the potential probes was plated on to regions where the potential gradient was small.

Conventional samples of type 3*a* were difficult to fabricate and were extremely fragile. In samples of type 3*b*, the high anisotropy ensures that planes which are normal to the current (basal planes) are also equipotential planes. Thus potential probes attached to the indicated surfaces measure the true potential which would exist even in the absence of the probes, the potential drop in directions normal to **c** being negligible.

The errors estimated by mapping the potential distribution on conducting paper are entirely negligible compared with the errors in measuring sample dimensions.

Cutting of specimens and attachment of electrodes

Stress-recrystallized graphite is easily deformed. Mechanical methods of cutting or of contact application can therefore result in inhomogeneous current flow. To minimize this risk, the following procedures were adopted:

For measurements of basal plane properties, cleaved disks of graphite (0·05 cm thick) were glued to stiff, thin paper with a cellulose cement, and the bridge-shaped outline (*a*) (figure 2) was cut by a fine stream of air-carried abrasive. Cut specimens were washed in acetone, dried, and painted with red varnish leaving only exposed regions to be copper plated.

In preparing specimens for c-axis measurements, a slab with oriented parallel sides, with prism faces exposed, was first cut by air-abrasion from a right cylinder held under a light constraining pressure. The outlines of configuration (a) were then cut in a continuous motion with the jet directed in the sense of arrow A (figure 3). Electrode surfaces were then roughened and were copper plated for 12 to 24 h in 10 % $CuSO_4$ solution containing 1 % H_2SO_4, by a current density of 1 mA/cm^3. Plating occurred preferentially on prism faces (plane edges); thus to ensure a strong coherent deposit on to basal plane surfaces, these were usually first roughened by air abrasion.

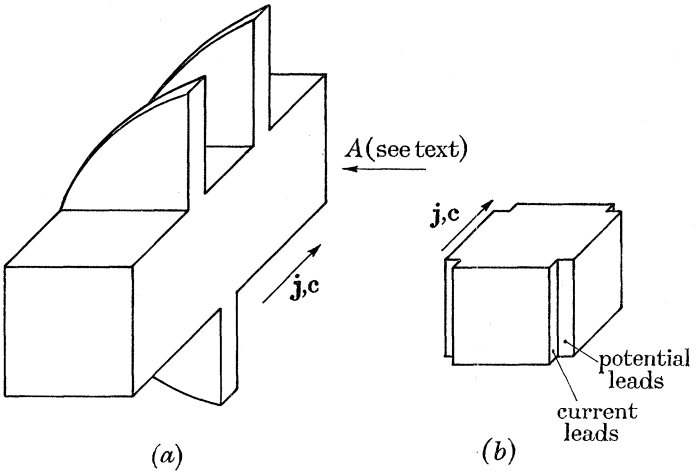

FIGURE 3. Sample shapes for c-axis measurements. (a) This conventional 5-point sample conformation was occasionally used, but was difficult to cut, fragile, and required carefully tapered potential probes. (b) This square conformation was simpler to cut, and stronger than 3a. It placed fewer restrictive requirements on the potential probe circuits.

After washing and drying, the copper was carefully tinned and leads were soldered on. Three or four copper leads (40 or 45 s.w.g.) served for the current input, and other leads were 45 s.w.g. copper; copper–constantan thermocouples were 45 s.w.g.

The general suitability of these techniques was confirmed by the high reproducibility of the data. No spurious or erratic effects were observed, even during cyclic changes of temperature. By shunting the potential probes with a low resistance circuit such that current was drawn through them, the interface contact resistances were shown to be negligible compared with the c-axis resistance of the sample.

Specimen mount, cryostat and magnetic field

In its final form, the specimen mount permitted rotation about a vertical axis at all temperatures and field strengths. Rotation to adjust the orientation about a horizontal axis could only be operated at room temperature.

The mounted specimen was housed in a cryostat of conventional design, operated at fixed temperatures between 4·2 and 300 °K. The specimen chamber of the cryostat could be filled with hydrogen or helium gas, or liquid refrigerant, or could be evacuated as required. Heat leaks were reduced to a minimum to permit simple measurements, e.g. of conductivity, during warming or cooling between fixed point temperatures. Temperatures were measured by means of a copper–constantan thermocouple calibrated at fixed points

down to the triple point of nitrogen, using tables for interpolation, and extrapolation to lower temperatures. The cryostat was mounted between the poles of an electromagnet (4 in. diameter, 2 in. gap). Magnetic fields (100 to 6700 G) were measured with a calibrated Hall probe.

Methods of measurement

After preparation, bridge shaped specimens for basal plane measurements were mounted in the 5-point configuration (figure 2*a*). Constant currents used were stabilized to $\pm 0{\cdot}01$ %. Voltages were measured to 0·2 μV on a galvanometer with a sensitivity of 12 mm/μV and an internal resistance of 33 Ω.

TABLE 1. CHARACTERISTICS OF STRESS-RECRYSTALLIZED GRAPHITES WITH INCREASING PERFECTION

sample no.	preparation no.	preparative conditions (°C) (hot press/anneal)	decrease of length on hot pressing (%)	density (g/cm^3) $\pm 0{\cdot}001$	$\left(\frac{d\rho_a}{dT}\right)_{300\,°K}$ (10^4 degK)	ρ_a(295 °K) ($10^{-5}\,\Omega$ cm)	$\frac{\rho_a(77)}{\rho_a(295)}$	$\frac{\rho_a(273)}{\rho_a(77)}$
SA 4	IFP 39	2800/—	17·2	2·258	−2·9	5·10	1·27	—
*IFP 41	IFP 41	2800/—	17	2·257	3	5·15	—	—
SA 7	IFP 36	2800/—	17·2	—	4	5·41	1·01	—
*IFP 56	IFP 56	2800/—	22·1	—	5	3·7	—	—
*†SA 22/SC 11	IFP 53	2970/3500	24·9	2·266	6·1	3·94	0·762	—
†SA 13/SC 10	IFP 52	2850/3250	23·3	2·265	6·4	4·10	0·742	—
†SA 11	IFP 45	2850/3300	—	2·233	6·5	4·51	0·75	—
SA 14	IFP 43	2850/3500	23·6	2·266	7·1	4·14	0·745	—
SA 23 } SC 12/14	IFP 46	2850/3500	20·1	2·260	8·55	3·79	0·715	—
SA 24 } SC 12/14	IFP 46	2850/3500	20·1	2·260	8·65	3·67	0·715	—
SA 20/SC 8	IFP 51	2850/3500	22·6	2·265	8·7	4·42	0·71	—
SA 15	IFP 41	2800/3500	17	2·257	9·3	3·91	0·675	—
SA 18	IFP 62	2900/3200	25·3	2·26	—	—	—	—
SA 19	IFP 62	2900/3500	25·3	2·26	—	—	—	—
SA 8	HTM	annealed at 3500	—	2·19	9·4	4·04	0·66	—
SA 21	IFP 64	2850/3500	23·0	2·26	10·7	3·59	0·625	—
SA 12	type B deposit (3600 °C) (see text)		—	2·25	11·0	4·00	0·625	—
*IFP A57	IFP 57	2850/3500	21·1	2·26	11·6	3·45	—	—
SA 26 } SC 15	JHP 1 } JHP 1	2850/3500	26·4	2·26	11·7	4·43	0·584	1·675
*‡SA 29 } SC 15	JHP 1 } JHP 1	2850/3500	26·4	2·26	11·7	4·08	—	1·685
SA 30 } SC 15	JHP 1 } JHP 1	2850/3500	26·4	2·26	—	4·11	—	1·685
SA 20 (N) SC 8 (N)	IFP 51	2850/3500	22·6	2·265	−18·1	—	—	—

* Basal plane scattering lengths L_a estimated from thermal conduction, electron microscopy and mean mobility are: IFP 41, 0·9 μm; IFP 56, 1·2 μm; SA 22, 1 μm; IFPA 57, 2·2 μm, SA 29, 2 μm.

† High concentration of soot nuclei which in SA 11 (IFP 45) caused partial loss of density on recrystallization. Sample SA 22 (IFP 53) did not show any plane rippling.

‡ Values of $\rho_a(295)/\rho_a(4{\cdot}2)$ for SA 24 and SA 29 are 4·38 and 13·3 respectively compared with the single crystal values Kinchin (1953) 12; Soule (1958) EP 7 16·7, EP 14 37·0; Primak & Fuchs (1954) 15.

For thermoelectric power measurements, a small constantan heater was wound on to the sample near one end, and the copper potential leads were replaced with 40 s.w.g. copper–constantan thermocouples.

The position of the specimen was normally first adjusted by eye, then by determining maxima and minima in the galvanomagnetic effects at room temperature as the sample was subjected to various rotation schemes:

(1) Position T_1 with current along the basal planes with magnetic field parallel to the c axis, $[\mathbf{a}\|\mathbf{j}\perp\mathbf{H}\|\mathbf{c}]$ rotating to position T_2 with current along the basal planes and magnetic field perpendicular to the c axis and to the current $[\mathbf{a}\|\mathbf{j}\perp\mathbf{H}\perp\mathbf{c}]$.

(2) Position T_1 (defined as in 1) rotating to the L longitudinal position $[\mathbf{a}\|\mathbf{j}\|\mathbf{H}\perp\mathbf{c}]$.

(3) A third rotation from T_2 to L was only rarely employed.

For c-axis measurements, because of the random orientation of the a axes of the constituent crystallites within a plane, only one longitudinal and one transverse orientation need be taken into account. Accordingly, specimens were mounted in the cryostat, using room temperature magnetoresistance to guide their orientation, in such a way that rotation could be imposed between

$$[\mathbf{H}\|\mathbf{j}\|\mathbf{c}] \equiv L \quad \text{and} \quad [\mathbf{H}\perp\mathbf{j}\|\mathbf{c}] \equiv T$$

positions. Currents used were in the range 3 to 5×10^{-2} A.

Results

Table 1 records the specimens investigated, with significant characteristics of the stress-annealing used. The sequence follows a trend of increasing crystalline perfection, assessed mainly from the temperature coefficient of resistivity $(\mathrm{d}\rho_a/\mathrm{d}T)_{300\,^\circ\mathrm{K}}$ at room temperature. Preparation numbers (IFP) serve to facilitate comparisons with previous publications.

Materials also used for a (shorter) series of c-axis measurements are given a second sample number (SC) in table 1.

Basal plane resistivity

To permit a general survey over all the specimens, the reduced resistivity $\rho_a(T)/\rho_a(295)$ is plotted (figure 4) as a function of the temperature T. For most of the samples data were recorded from 300 °K to 77 °K, but this limit was progressively extended downwards to 50 °K, 4·2 °K and about 1·2 °K for materials of particular interest. Samples SA 26, SA 29 and IFPA 57 (not shown) approximated closely to a good natural graphite crystal EP 14 (Soule 1958). For SA 24, which was considerably less perfect, the resistance was measured down to 1·6 °K. In agreement with other work (Soule, McClure & Smith 1964) its resistance apparently became constant below 4 °K (not illustrated in figure 4).

Three of the preparations listed in table 1 (IFP 41, IFP 56 and IFPA 57) were further characterized by thermal conductivity measurements from which estimates of boundary scattering lengths L_a could be made (Hooker *et al.* 1965*a*) (cf. table 1, footnote). These scattering lengths can be broadly correlated with values estimated from electrical conductivities. For the best specimens (SA 12/26/29), a boundary scattering length is found between 2 and 3 μm, in agreement with electron microscopy evaluations.

Room temperature resistivity, temperature coefficients, resistance ratios and estimated values of L_a are included in table 1.

It should be noted that cyclic applications of pressure on c-axis conductivity at 300 °K gave fully reversible results with the present materials (see also Spain *et al.* 1965). Plots of the pressure dependence, which showed an increase in conductivity with increasing pressure, were linear and passed through the origin. The high density of these materials precludes the presence of voids, and the behaviour under pressure is evidence that any

PHILOSOPHICAL TRANSACTIONS OF THE ROYAL SOCIETY A MATHEMATICAL, PHYSICAL & ENGINEERING SCIENCES

microcracks of near-molecular dimensions, considered to be present in some graphites, did not affect the present results appreciably. This contrasts with the more prominent role which must probably be attributed to such cracks in graphites of less perfect texture and lower density as used in some other work. For such materials, application of pressure gives rise to non-linear reductions of resistivity, and irreversible changes are observed that may be attributed to the collapse of voids.

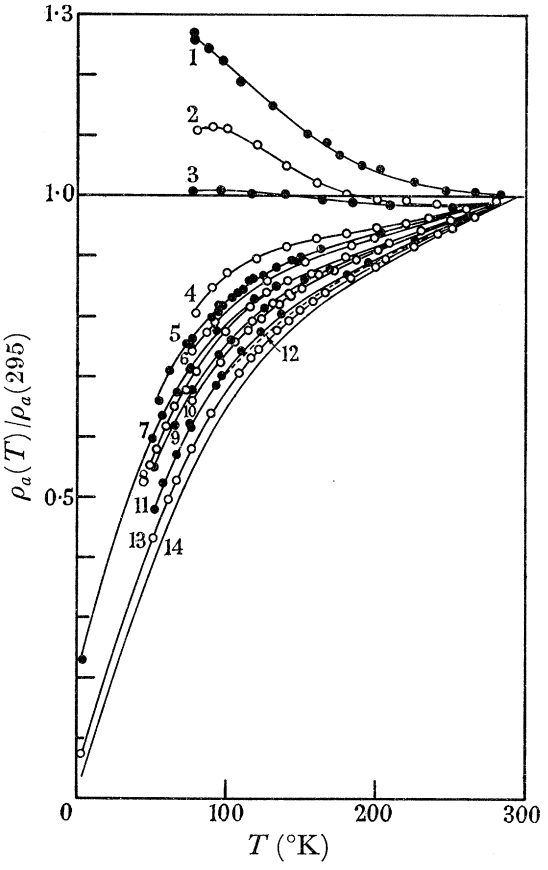

FIGURE 4. Reduced resistivity $\rho_a(T)/\rho_a(295)$ in the basal plane direction plotted against absolute temperature for a sequence of hot-pressed samples. Plots include curves for stress recrystallized material, and for a good natural single crystal (EP 14, Soule 1958). Materials may be identified by reference to table 1. Curves are numbered in sequence downwards, in the centre of the figure, as follows: (1) SA 4; (2) IFP 41; (3) SA 7; (4) IFP 56; (5) SA 22/13/11—these three curves superimpose within experimental error. The materials are characterized by their soot content. (6) SA 14; (7) SA 23/24—superimposed; (8) SA 20; (9) SA 15; (10) SA 8—commercial pyrolytic graphite annealed at 3500 °C; (11) SA 21; (12) SA 12—stress recrystallized at 3600 °C, dashed line; (13) SA 26/29—superimposed; (14) EP 14—lowest full line omits data points. Material IFPA 57 is not illustrated, but the points for it scatter around the curves for SA 26/29 and for EP 14 above 90 °K.

Figure 5*a* records a general plot of *c*-axis resistivity as a function of temperature for a short range of materials used in the present work. Sample SC 10 probably contained graphitized soot nuclei, though the *c*-axis distribution as assessed by cleavage planarity is very narrow. Three samples SC 12, 8 and 15 form a close and regular sequence. The range of resistivity values is narrow. SC 15 corresponds with samples found to be near ideal in

basal plane properties; it may be inferred in the c-axis properties likewise, that SC 15 asymptotes to intrinsic behaviour for ideal graphite. Its resistivity was therefore measured to the lowest temperatures conveniently attainable by pumping on the helium cryostat (1·2 °K). As seen from the expanded plot in figure 5b, no further change in the resistivity could be detected below about 5 °K.

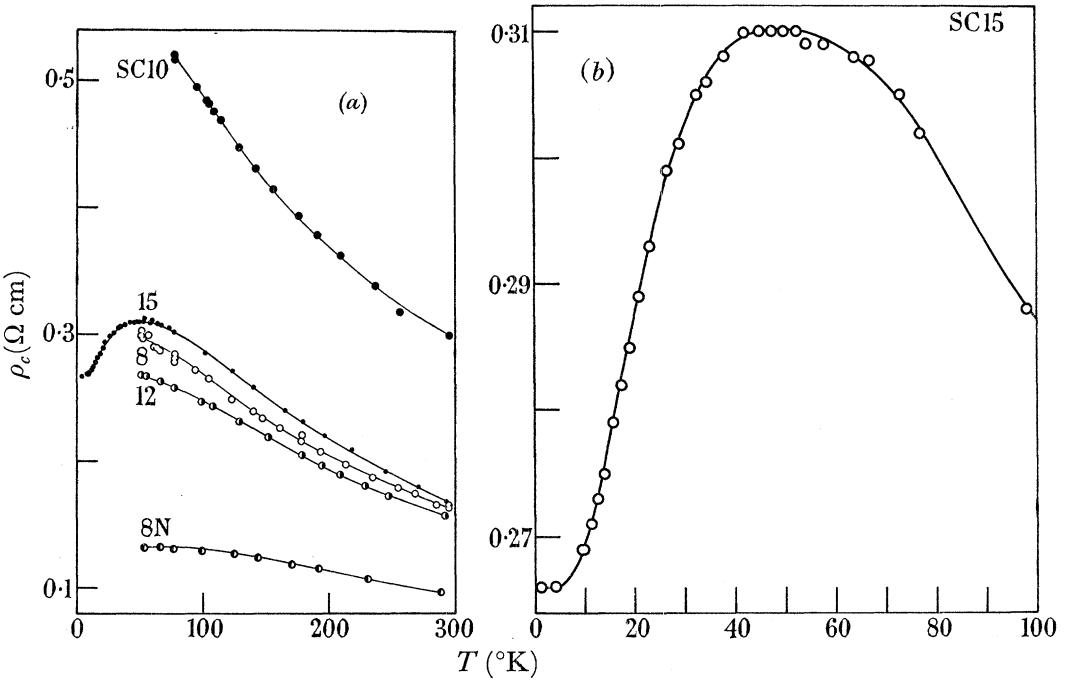

FIGURE 5. (a) c-axis resistivity of a representative series of materials also characterized by their basal plane transport properties. Materials SC 12, SC 8, SC 15 are in order of increasing crystalline perfection. SC 10 apparently falls out of sequence and SC 8 N shows the reduction of c-axis resistivity which is a consequence of neutron irradiation. (b) Low temperature c-axis resistivity of SC 15 on an expanded scale. Below 4·2 °K no further change in resistivity could be detected. This material is equivalent to the samples SA 26/29/30 (cf. table 1).

Magnetoresistance T_1

In the approach to ideal graphite, a second general assessment of sample quality (cf. Soule 1958) involves the magnetoresistance in the T_1 orientation, at a magnetic field fixed between 2500 and 3000 G, obtained as a function of temperature. To facilitate their presentation it is convenient to transform the data in terms of a mean mobility $\bar{\mu}$ for a simplified two carrier model (Soule 1958) with mobilities μ_1 and μ_2 for electrons (1) and holes (2) respectively, such that $\bar{\mu} = (\mu_1\mu_2)^{\frac{1}{2}}$ and

$$\bar{\mu} = \left(\frac{\Delta\rho}{H^2\rho_0}\right)^{\frac{1}{2}} \times 10^8 \text{ cm}^2\,\text{V}^{-1}\,\text{s}^{-1}. \qquad (1)$$

Plots are recorded for a sequence of stress-recrystallized graphites in figure 6. At about 77 °K ($\log_{10} T = 1{\cdot}886$) the trend of crystal perfection established on this basis (table 2) is comparable with that using the other general criteria described. Even amongst 'good' natural crystals (Soule 1958) variations are somewhat greater than for the best materials in the present series (e.g. SA 21, 12 or 26). Notwithstanding the well oriented but

polycrystalline texture of the synthetic materials, mean mobilities lie close to those for the natural crystal EP 14 above 77 °K. Table 2 also shows that at lower temperatures (< 50 °K) $\bar{\mu}$ for these materials falls below values for EP 14. At 4·2 °K magnetoresistances are no longer proportional to H^2, and values of $\bar{\mu}$ defined by equation (1), though useful for characterization, are not strict electrical quantities.

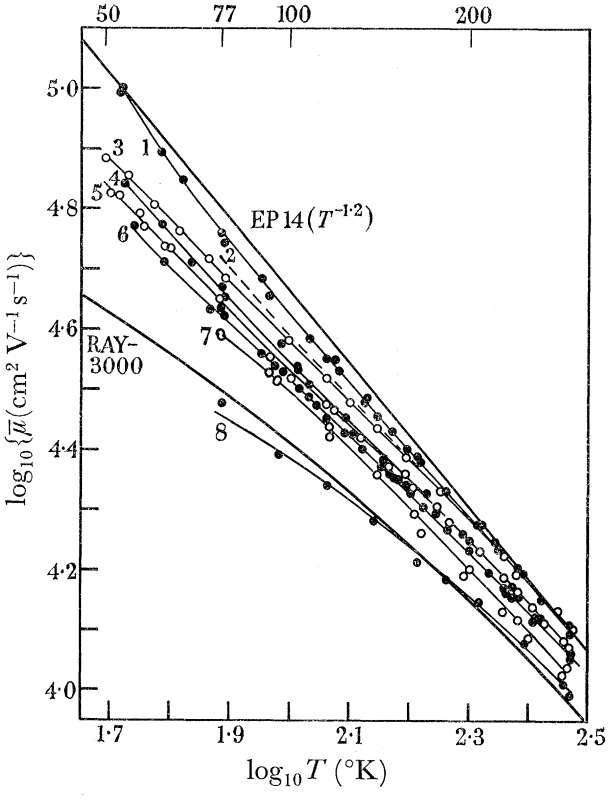

FIGURE 6. Logarithm of the mean mobility $\bar{\mu} = (\mu_1\mu_2)^{\frac{1}{2}}$ measured at 3 kG, plotted for a range of materials (sequences as in figure 4) against $\log_{10}(T\,°\mathrm{K})$. Limiting curves for a natural crystal at the top of the diagram (EP 14, Soule 1958) and for a pyrolytic graphite annealed at 3000 °C (RAY 3000, Klein 1964) at the bottom of the diagram. In general, hot-pressed and stress-recrystallized graphites used in the present work form a regular sequence between these two limits. They are numbered downwards as follows: (1) SA 26/12—superimposed; (2) SA 8—dashed line; (3) SA 20; (4) SA 21/15—superimposed; (5) SA 23/24—superimposed; (6) SA22/14/10—superimposed; (7) SA 11/13—superimposed; (8) SA 4. The materials can be identified by reference to table 1.

The T_1 magnetoresistance recorded by other authors (Klein, Straub & Diefendorf 1962, sample GE-ht-36A) agrees within a few parts per cent with the present values (samples SA 26, 29, 12). For another material (RAY 3000, Klein 1964) the complete plot virtually superimposes on our sample SA 4, which, though well oriented and dense, is considerably less perfect and still contains a high concentration of basal plane dislocations. The more extensive trends now established thus provide useful confirmation of calculated boundary scattering lengths of crystallites in various well oriented graphites, and support the general aim of the present researches to establish values for ideal graphite asymptotically. The

temperature dependence of $\bar{\mu}$ can be approximately represented by a combination of two relaxation processes (Klein 1964)

$$(\bar{\mu})^{-1} = \frac{m^*v}{e \times 10^7}\left\{\frac{1}{L_p} + \frac{1}{L_a}\right\}$$

with $m^*v = (2{\cdot}4 \pm 0{\cdot}8) \times 10^{-21}$ g cm/s, where L_p is the mean free path for electron-phonon scattering and L_a the boundary scattering length.

Application of this procedure to the data in figure 6 confirms that for SA 26, $L_a = 2\ \mu$m, whereas for SA 4 $L_a \sim 0{\cdot}8\ \mu$m. On this basis, other materials listed in table 2 have mean mobility values showing a regular trend in correlation with preparative conditions.

TABLE 2. AVERAGE MOBILITIES $\bar{\mu}$ (EQUATION (1)) FOR WELL ORIENTED GRAPHITES IN ORDER OF INCREASING PERFECTION

(Units of 10^4 cm^2 V^{-1} s^{-1})

sample	295 °K	77 °K	4·2 °K
SA 7	0·97	3·00	—
SA 13	1·09	3·89	—
SA 11	1·06	3·93	—
SA 22	1·13	4·19	—
SA 14	1·15	4·30	—
SA 24	1·19	4·46	18·3
SA 23	1·19	4·47	—
SA 18	—	4·55	—
SA 15	1·15	4·68	—
SA 20	1·26	4·85	—
SA 8	1·24	5·16	—
SA 21	1·25	5·50	—
SA 12	1·29	5·50	—
SA 26	1·24	5·85	—
SA 29	1·24	5·87	47·8
SA 30	1·24	5·85	—
natural crystals (Kinchin 1953)	—	—	46·2
EP 7	—	—	50
EP 11 (Soule 1958, figure 7)	1·3	—	190
EP 14	1·0	—	70

Field dependence of magnetoresistance T_1

Quite generally, an increase in scattering length or decrease in temperature increases the magnetoresistance. This is illustrated for a fixed field in figure 6 and for various magnetic fields at constant temperature in figures 7*a*, *b*. A simple power dependence $\Delta\rho/\rho_0 = aH^c$, where a and c are constants, with c ranging from 1·7 to 2·2, holds approximately above about 50 °K, though the logarithmic plots are not quite linear. Variation of the index c with temperature is in general agreement with measurements on a single crystal (Soule 1958, EP 7).

At 4·2 °K departures from linearity are more marked in the present plots (figure 7*a*). Again in agreement with single crystal data (on EP 7) (Soule 1958) the exponent changes continuously from about 2·0 at low magnetic fields, to about 1·2 at the highest field strengths studied. Though this is difficult to illustrate in the figure, the onset of Shubnikow–de Haas oscillations can be detected from apparent irregularity of the data for crystals SA 26/29 around $H = 4000$ G (figure 7*b*). Subsequent to obtaining the present data, these oscillations have been more fully verified with an X–Y recorder at 4·2 °K for SA 24

(Woore, unpublished observations). In figure 7, the general reduction of the exponent with increasing field appears to be due to the onset of saturation ($\mu H > 1$), which is, however, not fully attained for all carriers even at 24 kG with the best single crystals (Soule 1958).

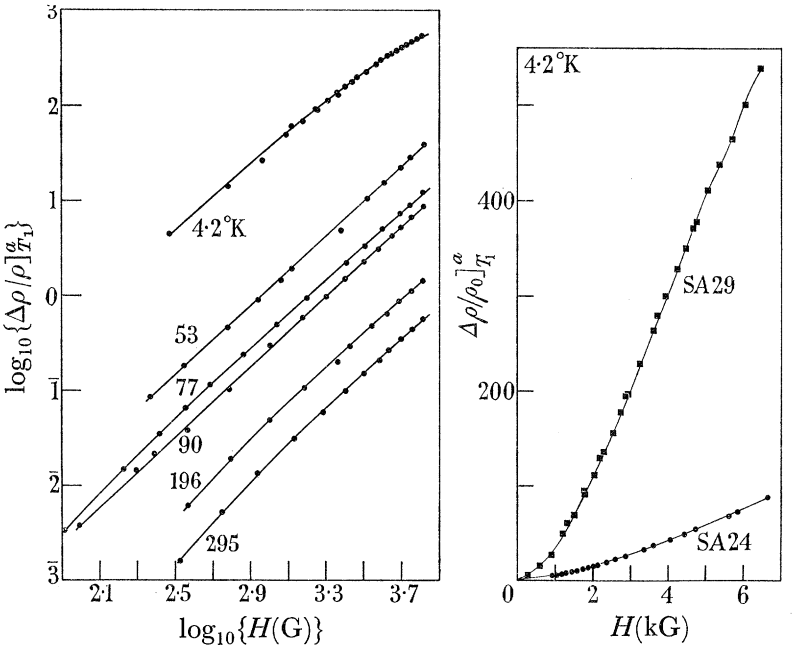

Figure 7. (*a*) Transverse magnetoresistance $T_1[\mathbf{a}\|\mathbf{j}\perp\mathbf{H}\|\mathbf{c}]$ for the best samples SA 26 and SA 29 plotted logarithmically as a function of magnetic field H for a series of temperatures. Samples SA 26 and SA 29 cut from adjacent positions in the same preparation were found to be identical within experimental error. Data at 4·2 °K were obtained on SA 29. Slopes of these curves are close to 2 at low fields, but reduce to 1·79 at higher fields; at the lowest temperatures the reduction, to about 1·2, is much greater. This parallels the behaviour reported for crystal EP 7 by Soule (1958).

(*b*) Transverse (T_1) magnetoresistances of samples SA 29 and SA 24 at 4·2 °K plotted against magnetic field (H). These illustrate the great sensitivity of this property to defect scattering. In SA 29 the apparent irreproducibility above 5 kG is in fact the onset of Shubnikow–de Haas oscillations, in confirmation of the long mean free path in this material.

This behaviour is more fully discussed below. In brief, the trends showed in the field dependence of magnetoresistance can be accounted for by a broad spectrum of effective masses of carriers, which extends to very low values for electrons (cf. Nozières 1958; Dresselhaus & Mavroides 1964): with the usual definitions

$$\omega_c = eH/m_c^*,$$

$$\mu = e\tau/m_c^*,$$

$$\omega_c\tau = \mu H.$$

Under conditions where orbital masses can be replaced by cyclotron masses, the product $\omega_c\tau$ exceeds unity at relatively low fields for the lighter masses. On closed surfaces this leads to progressive saturation starting with light carriers at low fields, and destroys any simple field dependence.

Magnetoresistances T_2 and L

With the specimen in the L position, the magnetoresistance was measured as a function of H for specimen SA 26 at 90 °K (figure 8). Independent measurements were also made at 77 °K of magnetoresistance as a function of field, for sample SA 24 held in the T_1, T_2 and L positions. Values of $\Delta\rho/\rho_0$ were so small for the T_2 and L positions that they could not be determined very accurately. However, $\Delta\rho/\rho_0]^a_{T_2}$ and $\Delta\rho/\rho_0]^a_L$ were found to be equal within experimental error (table 3).

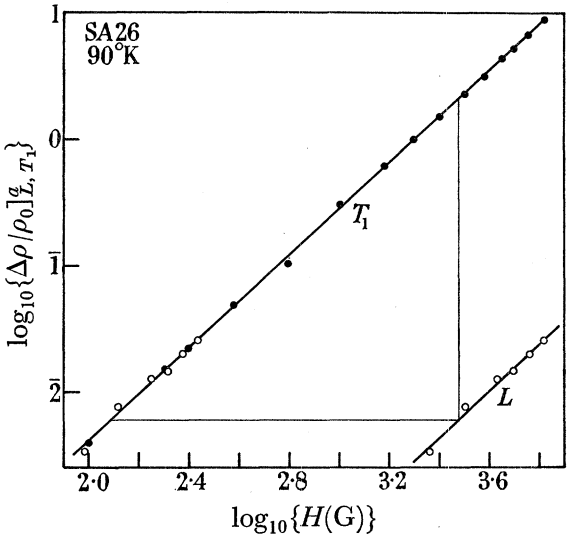

FIGURE 8. Transverse (T_1) and longitudinal (L) magnetoresistances for sample SA 26 at 90 °K plotted logarithmically against $\log_{10}H$, where H is the magnetic field in gauss. The magnetoresistance anisotropy can be read directly at 3 kG and the horizontal distance between the lines T_1 and L is then related directly to the overall angle $\phi_{(\mathrm{malorientation})}$ as described in the text.

TABLE 3. MAGNETORESISTANCE OF WELL ORIENTED GRAPHITE SA 24 AT 77 °K AT 3 kG

$\frac{\Delta\rho}{\rho_0}\Big]$	a, T_1	1·74
	a, T_2	0·0159
	a, L	0·0149

Magnetoresistance rotation diagrams

To locate magnetoresistance minima more accurately, values were measured for rotation between $T_1 \rightarrow T_2$ and $T_1 \rightarrow L$ positions. Data were obtained for samples SA 18, 19, 21, 22, 24, 26, 29 at selected temperatures between 4·2 and 295 °K. When plotted as $\Delta\rho/\rho_0$ against rotation angle, normalized with the value of $\Delta\rho/\rho_0]^a_{T_1} = 1$, the data for samples SA 21, 22, 24, 26 (figure 9) proved to be virtually indistinguishable. As might be expected from the field dependence of the T_1 effect, the curves cannot be analysed by the Voigt–Thomson expression for the property M as a function of angle,

$$M = M_1 \cos^2\theta + M_2 \sin^2\theta,$$

but empirically a satisfactory fit is obtained down to low angles if one uses an expression $M = \cos^{1.79}\theta$; the T_2 and L contributions being relatively small.

In a more sensitive examination, the data are replotted as the logarithm of the ratio $(\Delta\rho/\rho_0]^a_\theta)/(\Delta\rho/\rho_0]^a_{T_1})$ against the rotation angle θ. In this way, a considerable degree of irreproducibility becomes apparent near the minimum (figure 10). This irreproducibility stems from instrumental sources and also from ripples of longer wavelength (1 to 3 mm) that are not completely removed by hot pressing. Even when the macroscopic plane of the sample indicates that the magnetoresistance minimum should be attained, these ripples introduce resolved components from the high magnetoresistance direction, and raise the minimum. Finally, the intrinsic misorientation of the material arising from its mosaic structure affects the numerical values. Effects due to this are obtrusive, since they are superimposed on an *intrinsic* magnetoresistance in the T_2 or L positions which is unlikely to exceed about 10^{-5} of the intrinsic value in the T_1 direction.

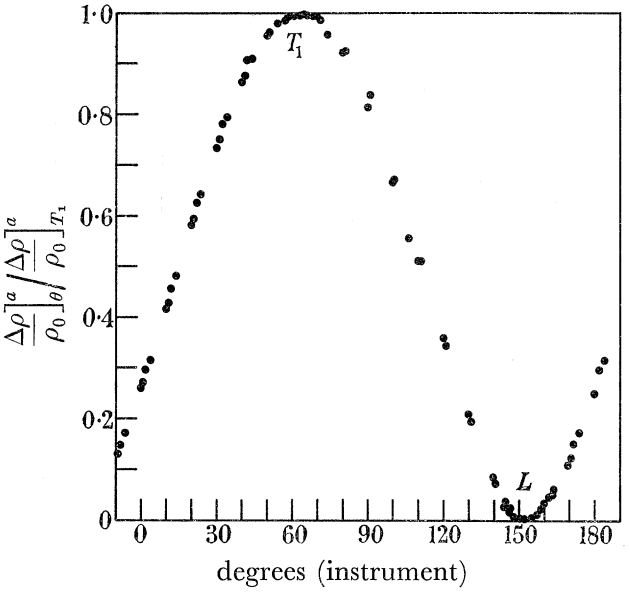

FIGURE 9. Dependence on angle of the basal plane magnetoresistance measured with the **H**-vector at an angle to the c-axis (T_1:$\theta = 0$; L:$\theta = \frac{1}{2}\pi$) divided by the T_1 magnetoresistance. Data for three materials SA 21, 22, 24 obtained at 77 °K and for SA 26 at 90 °K are included. Similar results are obtained for rotation from $T_1 \rightarrow T_2$. For clarity in presentation, about 40 overlapping data points have been omitted, and all other data points are given the same symbol. The half width of the negative half cycle is less than the half width of the positive half cycle, and these data can be fitted approximately by a function $\cos^{1.79}\theta$. The angular dependence near the maximum is weak.

With the degree of residual misorientation still present in the samples, our inference is that intrinsic contributions in the T_2 and L positions cannot at present be measured, since they are swamped by resolved contributions from $\Delta\rho/\rho_0]^a_{T_1}$. These raise the (apparent) values of $\Delta\rho/\rho_0]^a_{T_2}$ or $\Delta\rho/\rho_0]^a_L$ to between 0·1 and 1 % of $\Delta\rho/\rho_0]^a_{T_1}$.

A convenient method of representing the resultant average misorientation is to define it by the angle (ϕ (malorientation)) through which a perfect sample would have to be rotated in order to give the observed magnetoresistance at the minimum. Neglecting the (relatively minor) influence of malorientation on the absolute value of the magneto-resistance at the maximum (T_1), the field dependence of the magneto-resistance

is determined for nominal orientations T_1 and T_2 (or L), noting the anisotropy at, say, 3000 G. The translation along the log H axis which is required to bring the log $\Delta\rho/\rho_0]^a_{T_1}$ and log $\Delta\rho/\rho_0]^a_{T_2,L}$ plots into collinearity is calculated. The reciprocal of the anti-logarithm of the required displacement gives the sine of the overall malorientation angle as defined above.

This procedure has been used extensively with c-axis samples; by way of example, for SA 26 at 90 °K (figure 8) ϕ (malorientation) = 2·4°.

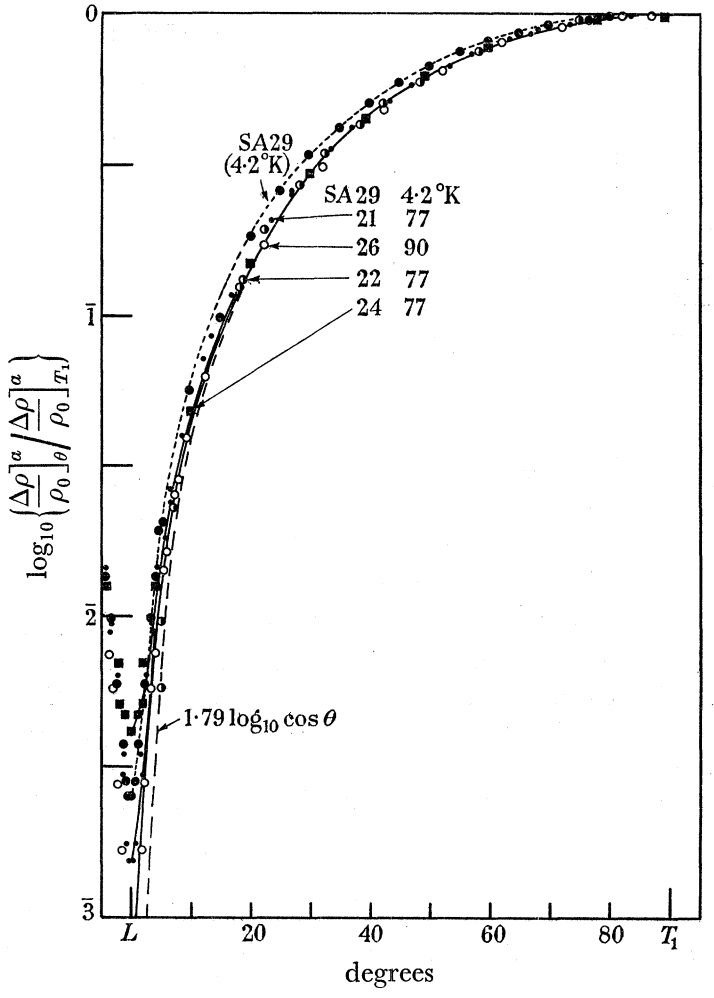

FIGURE 10. Logarithmic plot of the relative basal plane magnetoresistances $(\Delta\rho/\rho_0]^a_\theta)/(\Delta\rho/\rho_0]^a_{T_1})$ as a function of the angle θ between the magnetic field vector **H** and the c axis. The best materials SA 26 and SA 29 are included. Magnetoresistance anisotropies up to 460 are observed, most variations in behaviour appearing in the angular range within ±5° of the minimum (c-axis misorientation probably accounts for this effect—see text).

Anisotropy of magnetoresistance: effects of specimen rotation

c-axis conduction. The longitudinal magnetoresistance [**H**‖**j**‖**c**] is larger than is the transverse magnetoresistance [**H**⊥**j**‖**c**]. A typical rotation diagram, in which the ratio $(\Delta\rho/\rho_0]^c_\theta)/(\Delta\rho/\rho_0]^c_L)$ is plotted against angle (figure 11), includes data for one sample at 295 °K and for three samples at 78 °K. It is evident that the data superimpose within experimental error for angles more than 10 to 15° distant from the minimum, and that the

minimum is definitely sharper than the maximum. Irreproducibility becomes prominent near the minimum, as might be expected from its sharper form. This mode of representing the data brings out the (slight) effect of adventitious malorientation of the sample in attempting to optimise its longitudinal position. However, this would not greatly affect the measured anisotropy, so that experimental variations in this ratio can be attributed to internal misorientations or to intrinsic effects, but not to instrumental misalinement. No simple trigonometric power law could be fitted to the rotation diagrams.

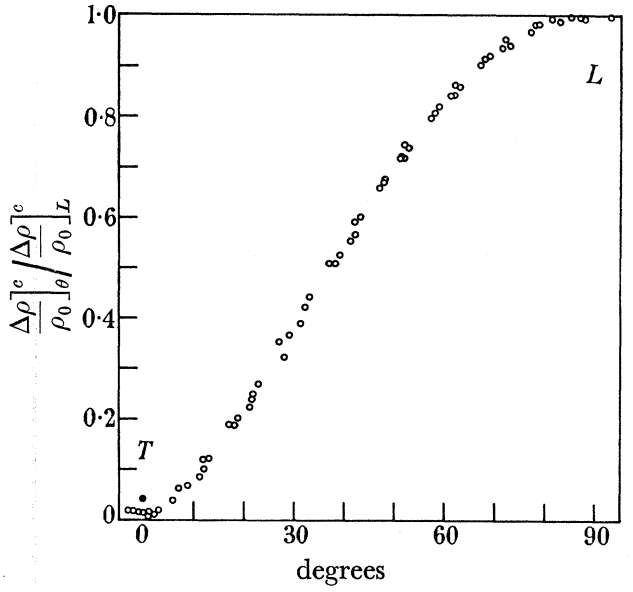

FIGURE 11. Anisotropy of magnetoresistance observed with *c*-axis samples on rotation in a fixed field from the *L* (**H**||**c**||**j**) to the *T* (**H**⊥**c**||**j**) position. About 100 experimental points have been omitted for clarity. It is seen that for three samples SC 8, 10, 14 at 77 °K and for one sample SC 8 at 295 °K plotted collectively the angular dependence of magnetoresistance is identical within experimental error, though the minimum is less deep for SC 15 (●) at 4·2 °K. This curve cannot be analysed by any simple trigonometric function. Note the weak angular dependence near *L*.

Depending on the sample and on the experimental conditions, the anisotropy L/T of magnetoresistance ranges between 25 and 460 (figure 12) with one value of 1820 (SC 11 at 298 °K).

Dependence on field strength and temperature is more complex for the longitudinal *c*-axis magnetoresistance [**H**||**j**||**c**] than for the T_1 basal plane values: At room temperature, plots (figure 13) show good concordance of the longitudinal magnetoresistance L of various samples (SC 10, 11, 12, 14, 15), but corresponding transverse values T vary widely. From the behaviour in the basal plane direction, SC 14 and SC 12 may be regarded as normal; plots for SC 10 and SC 11 may be anomalous, possibly because of retained soot nuclei, or because of the difficulty of locating the true minimum where the magnetoresistance is small. At 77 °K (figure 14*a*) and at 53 °K (figure 14*b*) corresponding families of plots again verify that samples of SC 12 and SC 14 show a limiting behaviour, with respect to all the materials studied. L/T anisotropies of magnetoresistance inferred from these plots are of the same order as from corresponding basal plane specimens, and

may provisionally be regarded as establishing the norm. But since anisotropy ratios L/T are about 10^2, by contrast with the theoretically expected 10^5, probably most of the observed effect $\Delta\rho/\rho_0]^c_T$ must be attributed to textural malorientation of individual crystallites, due to ripples in the deposited graphite. In fact, calculation of ϕ (malorientation) from the data of figure 14 give values ranging from 1° for SC 15 to 4° for SC 10.

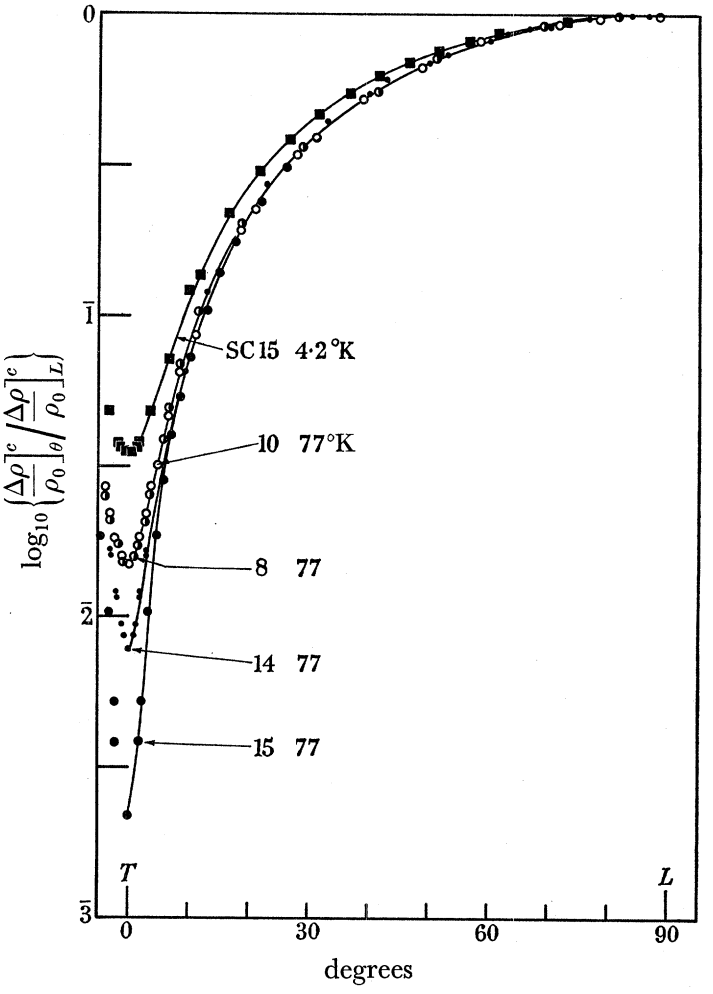

FIGURE 12. Selection of curves of magnetoresistance anisotropy $\Delta\rho/\rho_0]^c_\theta/\Delta\rho/\rho_0]^c_L$ plotted logarithmically against angle in order to bring out systematic differences near the T position. Data taken at 77 °K on SC 8, 10, 14, 15 agree within experimental error up to within 8° of the minimum, but at the minimum (T setting) the anisotropies diverge markedly. Better samples on the crystalline perfection sequence have the higher magnetoresistance anisotropy. On cooling sample SC 15 from 77 to 4·2 °K the magnetoresistance anisotropy decreases from 457 to about 25.

On cooling to 4·2 °K, the longitudinal magnetoresistance rises sharply. Clearly, an even steeper increase must occur for the nominal transverse magnetoresistance, since the anisotropy is reduced on cooling from 300 °K by a factor of about 18 for one of the best materials (SC 15) (figure 15). Field dependences at 4·2 °K (figure 16) are also quite different from those observed above about 50 °K. For the same material, *onset* of saturation of the longitudinal magnetoresistance can be perceived between 3000 and 4000 G. The

apparent reduction in anisotropy on cooling can again be explained if the transverse magnetoresistance is merely a resolved longitudinal effect, observed in effective fields which are inadequate to produce saturation.

Hall effects

Conventional Hall coefficients R_H measured in position T_1 with the current parallel to the basal planes were obtained at a series of temperatures between 4·2 and 300 °K and for magnetic fields up to 6700 G. General trends can be seen from figure 17, which permits comparisons over the whole range of temperatures between a sample of high perfection (SA 26 or SA 29) and a less perfectly ordered graphite (SA 24). For SA26

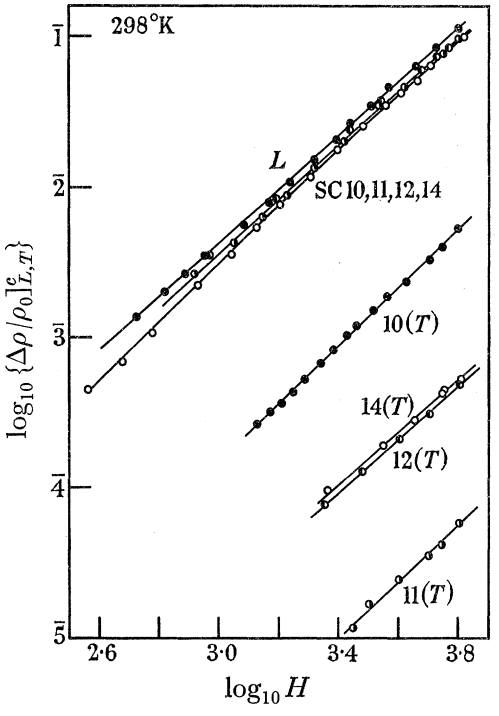

FIGURE 13. Longitudinal magnetoresistance in the *c*-axis direction compared for four samples with the transverse magnetoresistance at room temperature, plotted as a function of field. Reproducibility of the longitudinal effects is fair. Transverse effects are so small that there are difficulties in establishing true minima. Results for SC 12, 14 fall into the sequence established at lower temperatures, but curve SC 10 is unaccountably high and curve SC 11 low, though the *c*-axis distribution for SC 11 is very narrow.

noteworthy features are the negative value and weak field dependence of R_H at room temperature, and the appearance of a maximum at somewhat lower temperatures, with positive values of R_H over part of the plot. The highest positive value of R_H appears to be reached around 77 °K. By contrast, SA 24 shows the obvious differences that R_H never attains positive values, and that at temperatures where a maximum appears it occurs at higher magnetic fields than for SA 26. Comparative plots for samples covering a greater range of preparative conditions are recorded at 295 °K (figure 18) and 77 °K (figure 19) and 51 to 53 °K (figure 20). Particular features of these plots include the following:

1. At 295 °K the group of materials SA 8, 12, 22, 20, 19 (figure 18, curve *a*) show a larger negative Hall coefficient than any others, and have in common the significant

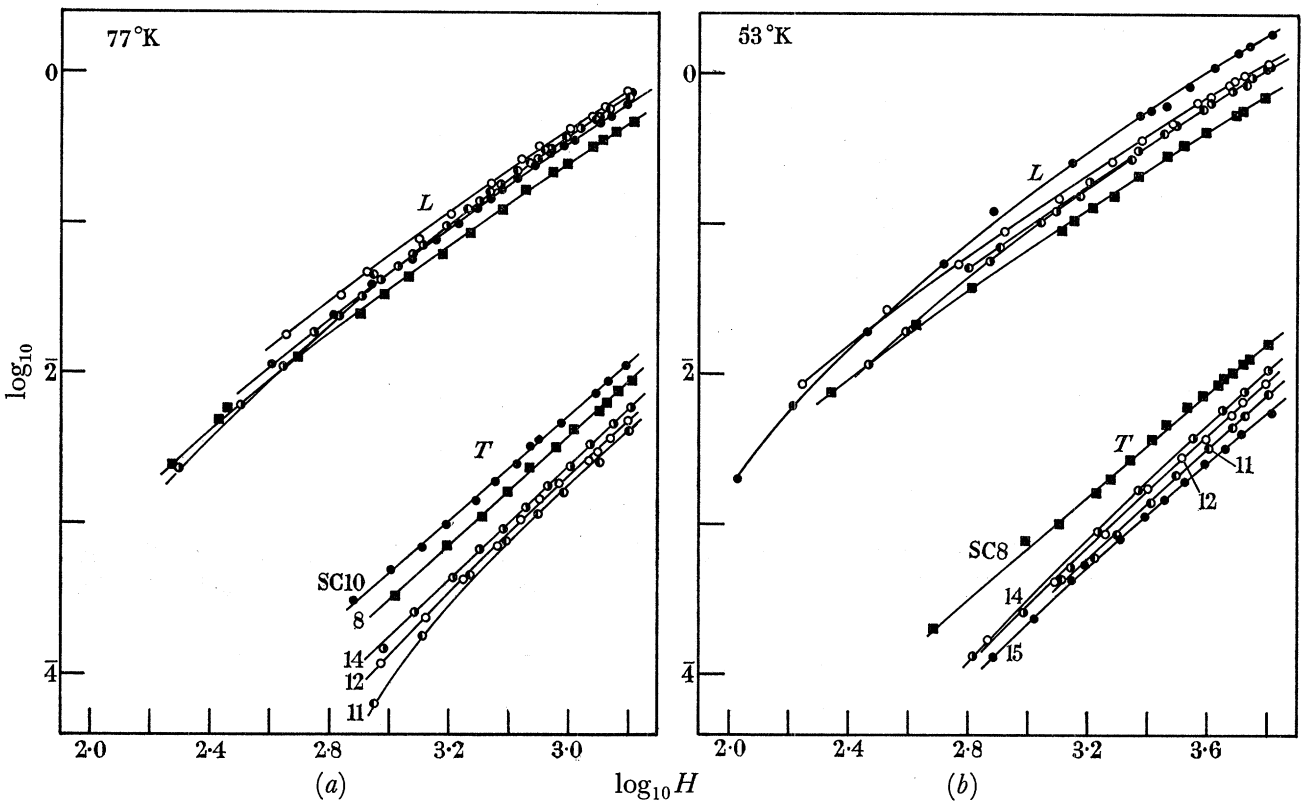

FIGURE 14. Longitudinal and transverse c-axis magnetoresistances of samples SC 8, 10, 11, 12, 14 at 77 °K (a) and of SC 8, 11, 12, 14, 15 at 53 °K (b) plotted as a function of magnetic field. These curves are analysed to determine ϕ (malorientation) by a lateral translation of the transverse curve (see text).

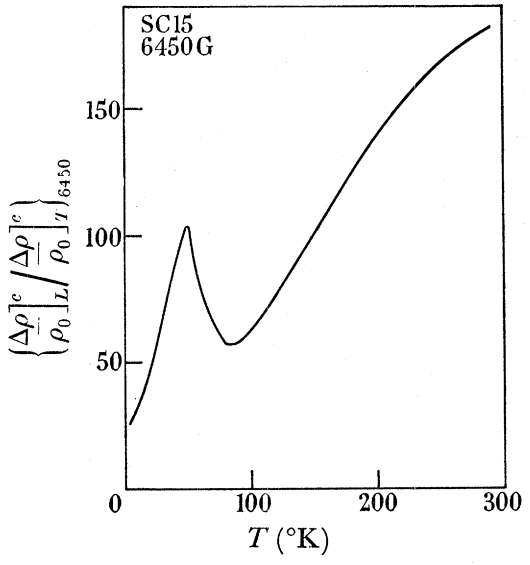

FIGURE 15. Magnetoresistance anisotropy of sample SC 15 at 6450 G as a function of temperature. A general fall is associated with saturation of the longitudinal effect as the temperature decreases. The peak at about 50 °K is authentic and corresponds with the onset of low angle scattering in the basal plane (see text).

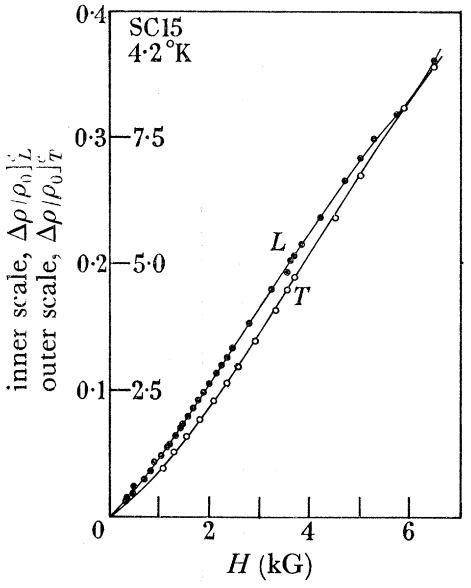

FIGURE 16. Longitudinal and transverse magnetoresistances at 4·2 °K of sample SC 15 as a function of magnetic field. Note the low anisotropy ($\sim$ 25) and the onset of saturation in the longitudinal effect.

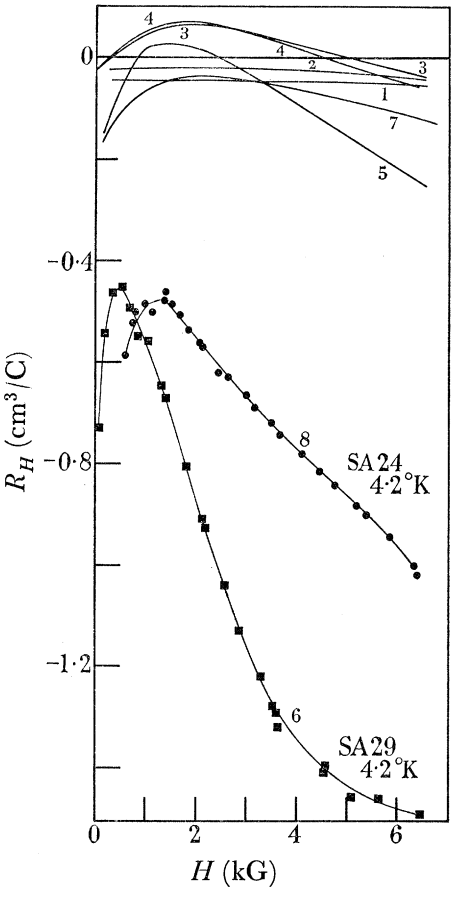

FIGURE 17. Basal plane (**H**||**c**) Hall coefficient R_H of two samples, SA 24 and SA 26/29 plotted as a function of magnetic field at a series of temperatures. SA 26: (1) 297 °K; (2) 194 °K; (3) 90 °K; (4) 77 °K; (5) 53 °K. SA 29: (6) 4·2 °K. SA 24: (7) 77 °K; (8) 4·2 °K. For the best material (SA 26/29) the R_H plots develop a positive maximum on cooling, which reaches its highest absolute value at about 70 °K. As the temperature is further lowered, the whole curve is displaced towards more negative values of R_H. The magnetic field at maximum R_H decreases steadily as the temperature is lowered. Zero field Hall coefficient is always negative. With sample SA 24 (which contains a higher defect concentration) the Hall coefficient never becomes positive.

feature of a high negative zero field value. In terms of the magnetoconductivity tensor analysis discussed below, this group of curves indicates a high concentration of light electrons associated with a high b value, where $b(=\mu_1/\mu_2)$ is the ratio of mobilities of the majority carriers (electron/holes). Material SA 21 (figure 18, curve b) has a low b value, and a high concentration of light electrons. The most nearly perfect materials SA 26, 29, 30 (figure 18, curve d) have a low b value and a low concentration of light electrons. Material SA 18 (figure 18, curve c) would appear to have an exceptionally low concentration of light electrons.

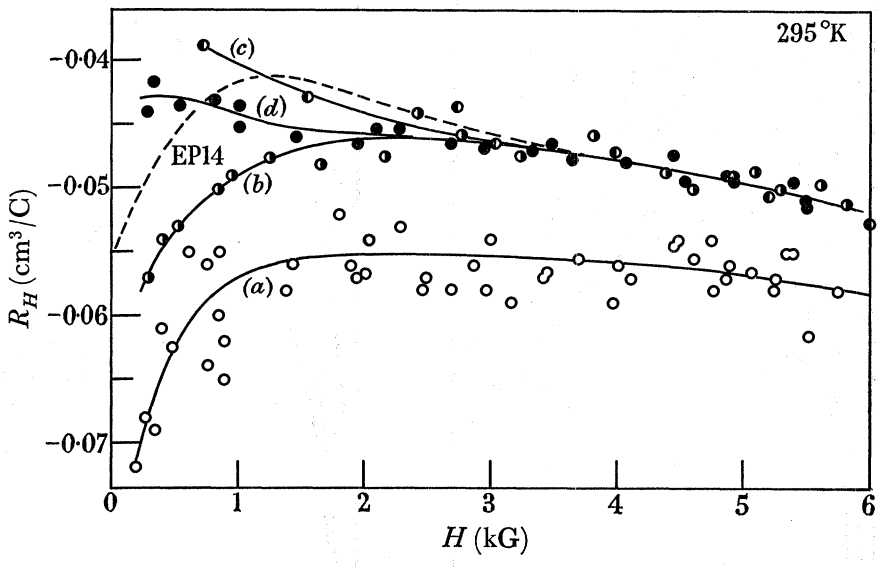

FIGURE 18. The Hall coefficient of a range of materials plotted against magnetic field at 295 °K. Four groups of curves can be distinguished: (a) SA 19, 20, 22, 12, 8. Data points (○) scatter badly, partly due to difficulties in measuring the magnetic field with a precision greater than ±5%. The negative-going branch for $H < 1000$ gauss is, however, authentic. (b) SA 21 (◑). Bad scatter is still observed, but the Hall coefficient is smaller than for group (a). (c) SA 18 (◐). As for (b) but the negative-going branch is not observed. (d) SA 26/29/30 (●). These samples were cut from adjacent positions in the same material. The precision of magnetic field measurements was greater (±2%). There are only slight indications of a negative-going branch at low magnetic fields. For comparison, data for EP 14 (Soule 1958) have been included. Note the excellent agreement with groups b, c, d for $H > 2000$ G.

Trends based on values of R_H (295) may be compared with the less sensitive 'crystalline perfection' scale based on reduced resistivity and mean mobility data (tables 1 and 2). If we omit materials SA 8, 12, which were not hot-pressed, the only new general feature apparent from the analysis of R_H (295) is that better materials tend to have smaller intermediate and zero field Hall coefficients. Close similarity between the best hot-pressed graphites and the single crystal value (EP 14) in the intermediate field range is noteworthy.

At 77 °K (figure 19) more data of higher reproducibility were recorded. For the systematic characterisation of defects, an important trend is that for the best samples, judged by other criteria, the Hall coefficient at its maximum is most strongly positive. It is most strongly negative in the least perfect materials. The field strength at which the maximum is found also increases monotonically with imperfection content. Other features

are that the slope for intermediate field strengths is rather insensitive to imperfection content, and that the difference between the zero field value R_0 and the value of the Hall coefficient at the maximum $R_{max.}$ increases with increasing imperfection content. Samples SA 22, 11, 13 (curves *j*, *k*, *l*) are believed to contain soot nuclei; samples SA 4 (curve *a*), 7

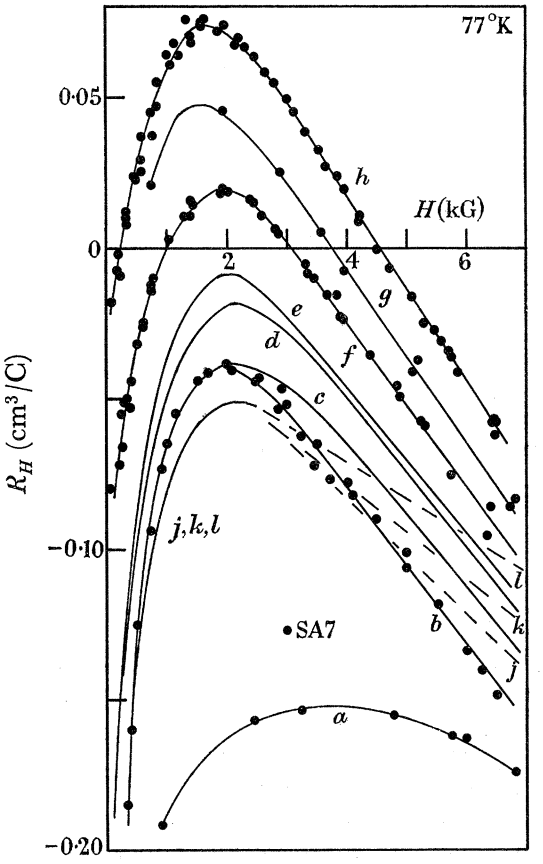

FIGURE 19

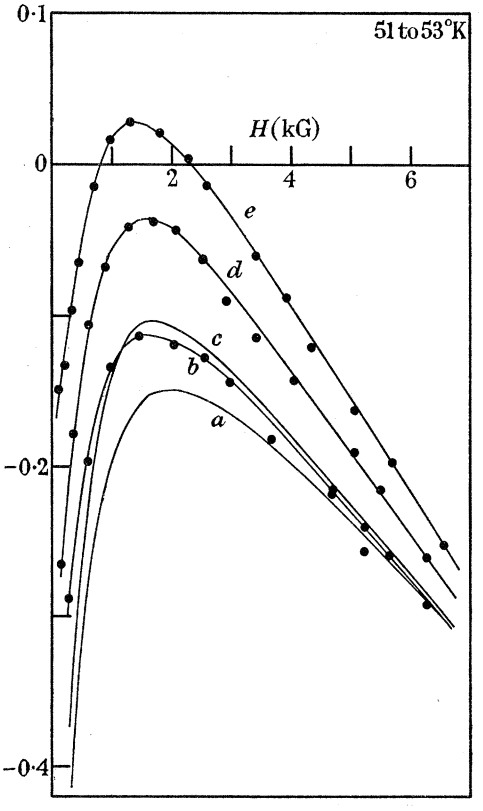

FIGURE 20

FIGURE 19. The full range of materials from SA 4 to SA 26/29/30 is included in a plot of the basal plane Hall coefficient at 77 °K as a function of the magnetic field. The curves group in two sequences: (I) (*a*) SA 4; (*b*) SA 20; (*c*) SA 24; (*d*) SA 15; (*e*) SA 18/19—superimposed; (*f*) SA 21; (*g*) SA 8/12—superimposed. Not hot-pressed. (*h*) SA 26/29/30—superimposed. The data for curve *h* are derived from three runs with the sample fixed (**H**||**c**) in a variable field, plus one run with the sample rotated from the $T_1 \rightarrow T_2$ position in a fixed field. (II) (*j*) SA 22; (*k*) SA 11; (1) SA 13. Materials in this group are believed to contain soot nuclei.

FIGURE 20. The Hall coefficient for a short series of samples at 51 to 53 °K plotted as a function of magnetic field (*a*) SA 22; (*b*) SA 20; (*c*) SA 24; (*d*) SA21; (*e*) SA 26.

(single point) were not annealed; these materials can be seen to behave rather differently from the others. Differential thermal expansion of the well oriented matrix and the graphitized soot nuclei must introduce high concentrations of basal plane dislocations; probably this accounts for the behaviour of samples SA 13, 11, 22. On cooling to 51 to 53 °K, all curves are displaced towards the negative region (figure 20), but are otherwise similar.

Hall coefficients recorded in figures 18 to 20 are not corrected for non-isothermal galvanomagnetic effects, which proved to be of little consequence in graphite. Because the

basal plane thermal conductivity of graphite is so large (Hooker *et al.* 1965*a*) it was not possible to eliminate the perturbing influence of the Righi–Leduc or the transverse Nernst–Ettingshausen effects by conventional techniques of field and current reversal. Calculations (cf. Jan 1957; Putley 1960) gave, as a typical example for $H = 5000$ G, $j = 0{\cdot}2$A; voltage differences ΔV in microvolts: Nernst–Ettingshausen, 10^{-1}; Righi–Leduc, 10^{-4}; Ettingshausen, 4×10^{-3}, compared with a Hall voltage of 50 μV.

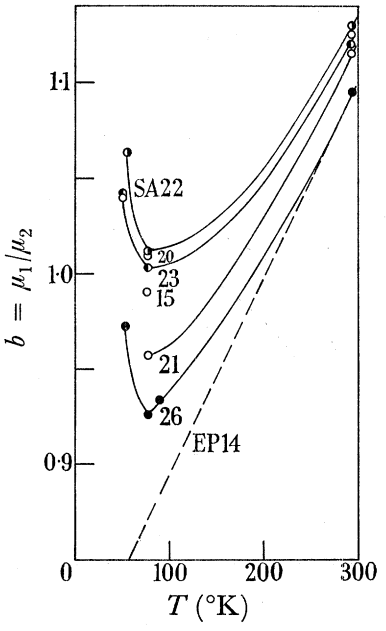

FIGURE 21. Mobility ratios $b = \mu_1/\mu_2$ calculated from intermediate field values of the Hall coefficient on the two carrier model, assuming $a = n_2/n_1 = 1$, plotted against temperature for a range of materials. (Soule's curve for EP 14, characterized by data points at 4·2, 77 and 300 °K only, shown for comparison.)

Dimensions of the sample were such that short-circuiting of the Hall voltage by the current electrodes was negligible ($< 0{\cdot}2\,\%$) (cf. Isenberg, Russell & Greene 1948; Drabble & Wolfe 1956), while the Hall angles were too small to cause short-circuiting at the probes (cf. Frederikse & Hosler 1957). Possible inhomogeneties of magnetic field ($\leqslant 1\,\%$ cm^{-1}) would affect the Hall voltage by less than 0·5 % at 4·2 °K; and less than 0·1 % above 50 °K (cf. Bate & Beer 1961). In confirmation, values of the magnetoresistance potentials reversed within experimental error on reversing the field.

Transformation of the Hall data by means of simple two carrier calculations assuming the ratio of carrier concentrations $a = n_2/n_1 = 1$ yield the ratio of mobilities $b = \mu_1/\mu_2$ at selected temperatures. As illustrated (figure 21), a minimum is found at about 70 °K, whose characteristics are correlated with increasing dislocation content of the materials.

In the c-axis direction, within the range of variables studied, Hall voltages proved to be linear functions of the magnetic field, for all the materials investigated. From plots of the zero-field Hall coefficient as a function of temperature (figure 22) it will be seen that at low temperatures the curves fan out, as might be expected for multi-carrier conductors in which the concentration and mobility of carriers depend on the texture of the material. Comparisons with the other electronic properties studied indicate that R_H may be more

PHILOSOPHICAL TRANSACTIONS OF THE ROYAL SOCIETY A MATHEMATICAL, PHYSICAL & ENGINEERING SCIENCES

discriminating in showing up differences in these respects. On a two-band model, plausible assumptions (cf. the behaviour of irradiated material below) are that for both carriers $n_i(c) = n_i(a)$. For $a = n_2/n_1 = 1$ as before, the expression $R_0 = (a-b^2)/n_1 ec\ (a+b)^2$ yields the result $b = (\mu_1/\mu_2) = 1{\cdot}034$ for material SC 8 at 90 °K. Three carrier calculations are postponed to the general discussion below.

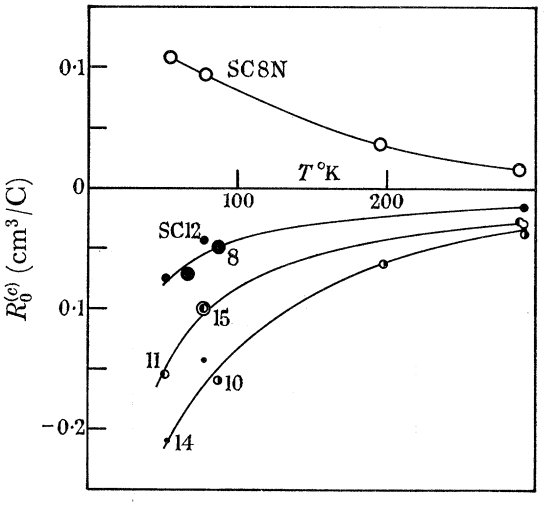

FIGURE 22. Zero field Hall coefficient for samples SC 8, 10, 11, 12, 14, 15 and 8 N plotted as a function of temperature. The Hall coefficient is positive for the neutron irradiated graphite SC 8 N. It is negative and varies in a irregular manner with unirradiated specimens. In all cases there is an increase in $R_0^{(c)}$ as the temperature is reduced.

Thermoelectric power

Plots of thermoelectric power S_a measured on various samples in the basal plane direction are recorded in figure 23. Data for specimens IFP 41, IFP 56 and IFP 57 (cf. table 1) were obtained in the course of thermal conductivity measurements (Hooker *et al.* 1965*a*). In all cases a maximum is found. At 300 °K the values of S_a converge, and also agree with previous data on less perfect graphites in the basal plane direction (Blackman *et al.* 1961).

With the present series of graphites, the thermoelectric power becomes strongly negative at low temperatures, in excellent agreement with other results obtained on graphite filaments (J. T. Meers quoted in McClure & Smith (1961) and private communication). A high content of imperfections causes an increase in the negative thermoelectric power between about 70 and 200 °K. The minimum previously reported (Blackman *et al.* 1961) at about 90 °K was not found with any of the present series of graphites. It seems possible that the specimen for which it was observed had a stratified structure arising from its mode of formation. A minimum must, however, appear at still lower temperatures, since theoretically $S_a \to 0$ as $T \to 0$. With the graphites studied by Meers a minimum of $-20\ \mu$V/degK was found at around 35 °K.

For specimen SC 8, various observations of thermoelectric power S_c in the c-axis direction are also available (figure 24). On a two-band model with $a = 1$, the small positive value of S_c at room temperature implies that holes are more mobile than electrons. As the temperature falls, S_c becomes negative, and the electrons must become more mobile than the holes. These conclusions are not entirely consistent with the zero field Hall

coefficients at high temperature; possibly the ratio $a = n_2/n_1$ decreases somewhat with rising temperature.

An attempt was also made to measure the so-called 'planar Hall effect' by rotating one specimen (SA 23) between orientations T_2 and L. No observable variation in the voltage drop could be detected at either 295 °K or 77 °K, in agreement with the expected low value of $\omega_c\tau$ in this orientation.

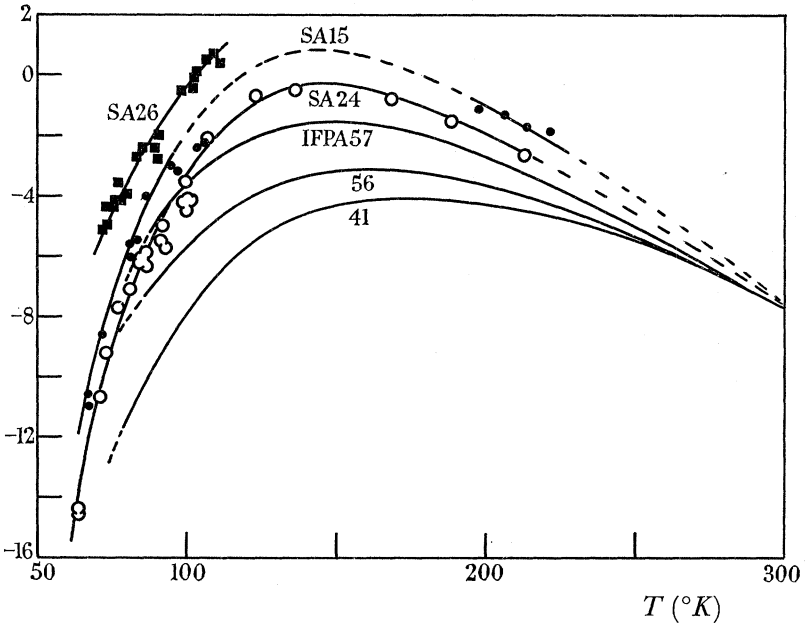

URE 23. Absolute thermoelectric power for basal plane samples. Curves IFP 41, IFP 56 and IFPA 57 (see text) and curves SA 24, 5 and 26 show an upward trend with increasing perfection.

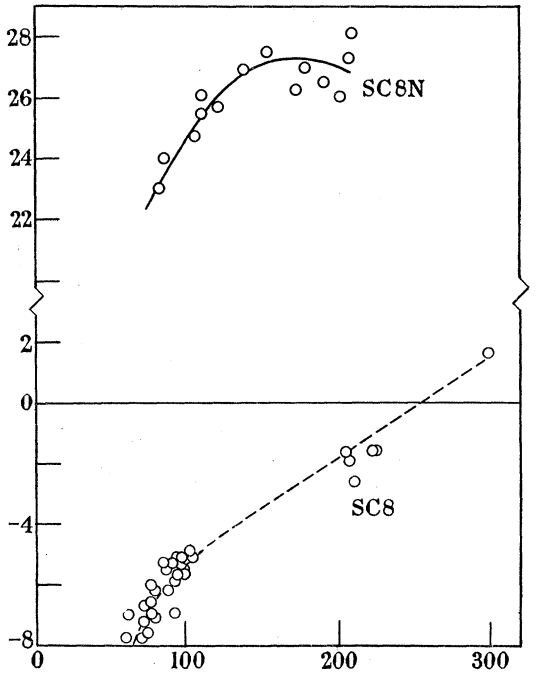

FIGURE 24. Thermoelectric power of SC 8 and SC 8 N.

Effects of neutron irradiation

As an extension to studies of trends in the electronic behaviour of a range of samples of near-ideal texture, useful additional information can be obtained by introducing a small number of defects which both scatter charge carriers and act as electron traps, by exposure to neutron irradiation. The graphite selected for irradiation (SC 8, corresponding to SA 20) proved to be less perfect than the best materials eventually available; nevertheless, comparisons of data in both principal crystal directions for this material before and after irradiation were very informative. Samples were irradiated in the reactor BEPO in a hollow fuel element at about 30 °C to a total fast neutron dose of about 10^{18} n.v.t. Effects in both directions are conveniently discussed together.

Basal plane direction

As illustrated (figure 25) specimen SA 20 N has a room temperature resistivity of $18 \times 10^{-5}\,\Omega\,\mathrm{cm}$; this is about four times as large as was found with SA 20, i.e. before irradiation. The temperature coefficient of resistivity is negative at least down to 60 °K. The thermoelectric power is large and positive (about 30 μV/degK), supporting the

conclusion obtained with synthetic graphite (Hennig & Hove 1956) that irradiation lowers the Fermi level. In conformity with effects expected from the introduction of scattering centres which impose a near-constant mean free path, the transverse T_1 magnetoresistance of SA 20 N is one to two orders of magnitude smaller than for SA 20, and much less

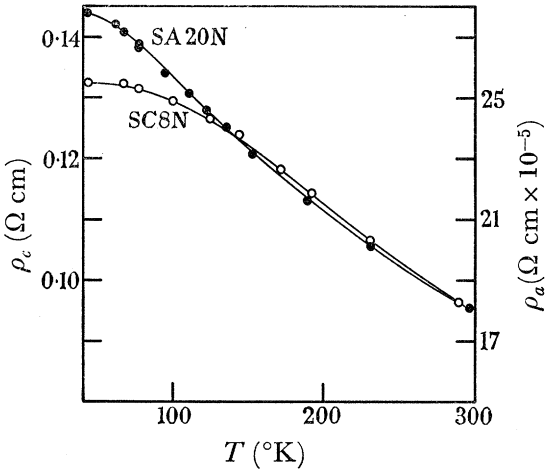

FIGURE 25. Electrical resistivity as a function of temperature for materials SA 20 N and SC 8 N. Dependence is practically linear above 130 °K.

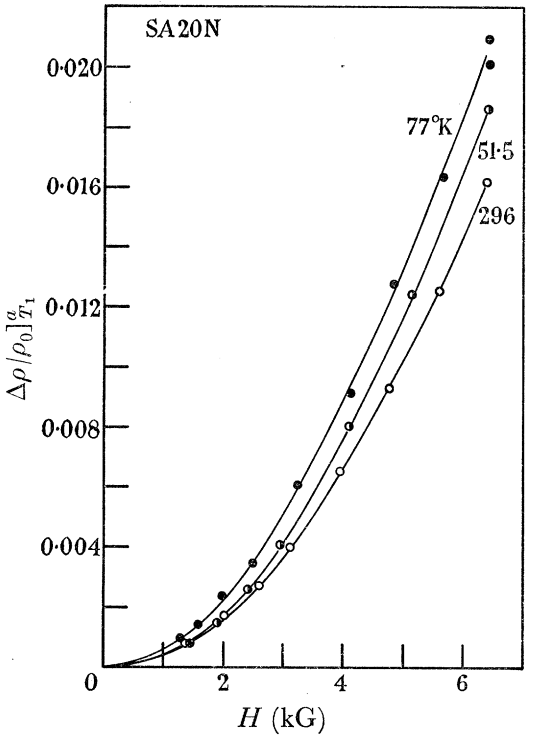

FIGURE 26

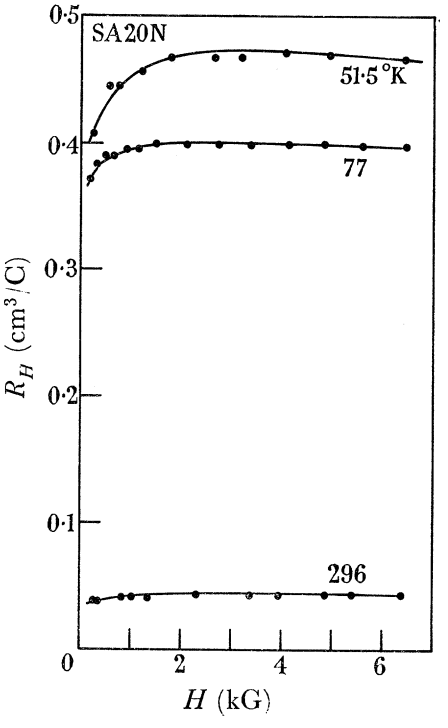

FIGURE 27

FIGURE 26. Transverse (T_1) basal plane magnetoresistance of SA 20 N plotted against the magnetic field. Dependence on temperature much weaker than for unirradiated material.

FIGURE 27. Hall coefficient of SA 20 N. This is only very weakly field dependent for $H > 2$ kG, indicating that positive holes predominate. At low fields the contribution from light electrons is still apparent and the saturation field $H_3 = c/\mu_3$ is larger than for unirradiated material.

dependent on temperature (figure 26). Calculations of a mean mobility, $\bar{\mu}$, do not apply to this case ($a = n_2/n_1 > 1$), but the results can be combined with Hall coefficient data to yield charge carrier concentrations and Hall mobilities.

Hall coefficients as a function of field are recorded at three temperatures for this neutron irradiated sample (figure 27). The near constancy in the intermediate field range suggests that the irradiated solid behaves as a single carrier conductor with $a = n_2/n_1 > b = \mu_1/\mu_2$ whence $R_0 = (n_2 ec)^{-1}$. Values of n_2 and μ_2 calculated on this basis are given in table 4.

A particularly interesting feature (figure 27) is that light electrons still appear to be present in the irradiated sample. A plausible estimate is $n_3 = 5 \pm 4 \times 10^{16}$ cm^{-3} at 51·5 °K, i.e. about the same value as before irradiation. It is evident that the contribution of light electrons increases as the temperature is reduced. Comparisons (figure 20, curve (*b*) and figure 27) indicate that the characteristic field H_3 is larger after irradiation.

c-axis direction

From comparison of the electrical resistivity as a function of temperature of samples SC 8 (figure 5*a*) and SC 8(*N*) (figure 25), it is evident that on irradiation the resistivity is *reduced* in the *c* direction; its temperature coefficient is also reduced. As a consequence, the anisotropy of resistivity, which was about 4×10^3 at 300 °K, and $12{\cdot}2 \times 10^3$ at 77 °K for the best unirradiated samples (SA 26 and SC 15), falls to about 520 over the temperature range (70 to 300 °K) for these irradiated materials (SA 20 N and SC 8 N) (figure 25).

This finding raises problems of mechanisms of *c*-axis conduction in irradiated material in acute form. It seems wholly plausible to postulate that static obstacle scattering (fixed mean free path) combined with a temperature dependent concentration of charge carriers can largely account for basal plane conduction as the temperature falls. However, it is not immediately apparent in what way the same mechanism can simultaneously increase the conductivity in the *c*-axis direction.

This situation led to consideration of the possible role of interstitial clusters formed by radiation, in which displaced carbon atoms act as 'bridges' in *c*-axis transport (Ammar & Young 1964). Whilst this role cannot be excluded, new information is provided by various effects of irradiation observed in the present work, as further detailed below.

c axis magnetoresistance

Sample SC 8 N was examined at 297, 77 and 53 °K. As with the equivalent material SA 20 N studied in the basal plane, the variation with temperature of the magnetoresistance obtained with **H**||**c** [*L for c axis*: T_1 *for basal plane*] is much less marked than with unirradiated material. Apparently radiation damage reduces the mean free path towards a value largely independent of temperature. Under these conditions, temperature variation of transport properties is determined mainly by the temperature dependence of the charge carrier concentration. Comparisons show that the magnetoresistance is reduced by a factor of about 100 by irradiation. In consequence, only very limited data could be obtained on the transverse effect T. These indicate a magnetoresistance anisotropy L/T of about 10^2 at 53 °K and about 10^3 at 77 °K, supporting previous conclusions when majority carriers predominate.

PHILOSOPHICAL TRANSACTIONS OF THE ROYAL SOCIETY A MATHEMATICAL, PHYSICAL & ENGINEERING SCIENCES

With irradiated material, the Hall coefficient in the basal plane is always positive and increases monotonically with reduction in temperature. Assuming the predominance of heavy hole carriers, the Hall coefficient is approximately given by $R_0 \simeq (n_2 ec)^{-1}$.

On this basis the approximate numbers of charge carriers n_2 and their Hall mobilities μ_2 are calculated to be as in table 4.

TABLE 4. CHARGE CARRIER CONCENTRATIONS AND HALL MOBILITIES IN IRRADIATED GRAPHITE—SAMPLES SA 20 N AND SC 8 N

	a		c	
T °K	$10^{-19} n_2$ (cm^{-3})	μ_2 (c.g.s.)	$10^{-19} n_2$ (cm^{-3})	μ_2 (c.g.s.)
51·5	1·3	$5{\cdot}20 \times 10^5$	2·8	502
77	1·5	$4{\cdot}52 \times 10^5$	3·3	424
296	1·7	$7{\cdot}28 \times 10^4$	21	93·9

GENERAL DISCUSSION

Electrical conduction in single crystal graphite has been discussed by other workers in some detail (Sugihara & Sato 1963; McClure & Smith 1961; Gerlach 1962). Interesting extensions of these theories are brought out by the deliberate asymptotic approach to perfect crystallinity aimed at in the present research.

One outcome of studies of trends in properties in relation to texture is to establish and validate norms for ideal crystalline graphite. For basal plane properties fairly complete systematic studies of trends could be carried out. From the c-axis data, only short sequences of samples (table 5) can be arranged.

Despite the shorter sequences available, the same trend of sample numbers towards perfect crystal behaviour is found as from basal plane properties. Thus, for example, SC 8 is a graphite of moderately defective texture, whereas SC 15 or SC 14, which is closely similar, is a graphite of high perfection with respect to c-axis properties. It follows that the zero field Hall coefficient $R_0^{(c)}$ of ideal graphite is less negative at low temperatures, than for imperfect graphites.

Path tortuosity effects

Careful scrutiny is needed to verify that the c-axis data recorded refer to electrical transport properties genuinely normal to the basal planes, and therefore warrant interpretation in terms of the properties of Fermi surfaces. One obvious criticism could be based on the fact that the anisotropy of graphite is so large that even slight c-axis misorientation can render attempts to measure valid c-axis properties ineffective. As an extreme instance, if the ratio of resistivities ρ_c/ρ_a were infinite, the low resistance basal plane paths would completely short-circuit non-conducting c-axis paths, and specimen properties would be determined merely by 'tortuous path' summations of basal plane properties.

It can readily be verified that this extreme case does not apply. A good test is that in recrystallized material the temperature coefficient of resistivity in the basal plane is positive throughout the temperature range studied (4·2 to 300 °K). On the other hand, observed 'c-axis resistivities' show a negative temperature coefficient from 300 °K down to 60 °K, becoming positive only at lower temperatures. Thus the measured property must involve a major contribution from true c-axis conductivity. The anisotropy, though

large, cannot be sufficiently great to invalidate determinations of c-axis properties on the materials studied.

Although the above conclusion seems reasonable, if for some unforeseen reason intercrystalline boundaries made a substantial contribution to the resistivity, the observed c-axis temperature coefficient could no longer be used in support of the present conclusion. Since the whole range of samples shows much the same negative temperature coefficient of c-axis resistivity (figure 5a) even though the samples vary in density, it is unlikely that intercrystalline boundaries in series with tortuous basal plane paths account for observed c-axis resistivities. The strongest evidence that basal plane conduction does not contribute to c-axis conduction by way of tortuous paths is provided by the neutron irradiated samples (SA 20 N and SC 8 N), for which an *increase* in basal plane resistivity is accompanied by a *decrease* in c-axis resistivity.

TABLE 5. TRENDS OF INCREASING PERFECTION BASED ON c-AXIS PROPERTIES

property	$\Delta\rho/\rho_0]_L^c$		$\left.\frac{\Delta\rho}{\rho_0}\right]_L^c \Big/ \left.\frac{\Delta\rho}{\rho_0}\right]_T^c$	$R_0^{(c)}$
ρ_c	53 °K	77 °K		
12	8	8	8/10	8/12
8	14/11	10	14	11/15
14/15	12	11/14	12/11	10/14
—	15	12	15	—

The sample numbers SC are arranged in order of increasing perfection reading downwards.

Comparisons between sample SA 20 (table 6) and SA 20 N (table 4) show that irradiation raises the concentration of charge carriers contributing to basal plane transport by a factor of about 3·3 at 77 °K, whereas the increase in conductivity in the c-axis direction after irradiation is only two-fold. This could be explained if the same number of charge carriers are actually operative in both basal and c-axis directions, but with the mean free path fixed by sample topography. The apparent decrease of mobility on irradiation can be attributed to the fact that $(m_2^*)^{(c)}$ at $14m_0$ is about twice $(m_1^*)^{(c)}$ at about $5{\cdot}7\ m_0$; thus the carriers in SC 8 (N) have about half the mobility of the carriers in SC 8. A corollary of this view is that in the c-axis direction in materials of the present high quality studied, the mean free path changes but little above 50 °K. Reasonable estimates (for SC 15) are $\lambda_c = 8$ Å at 50 °K and 4 Å at 300 °K. This supports the assumption that between 50 and 77 °K, where the data are most accurate, the number of charge carriers available for basal plane and c-axis transport is equal within experimental error.

Band characterisation in relation to defect structures in graphites

Simple transformations of the experimental data have already been discussed above.

As a basis for fuller characterization, the Slonczewski–Weiss model of the energy bands may be used (cf. McClure 1957, 1964; Dresselhaus & Mavroides 1964; Slonczewski & Weiss 1958). For convenience, the general features of the model are illustrated in figure 28a–d.

The electron Fermi surface is of small cross-section and cuts the hexagonal face of the Brillouin zone. The small volume outside the first zone is accounted for by the single degenerate level E_1 which lies Δ energy units below the doubly degenerate levels E_3 at the zone face, electrons being characterized for energies greater than zero. These second zone

electrons occur at the light mass extremity of the effective mass spectrum (figure 28*c*) in the basal plane. The question of spin-orbit splitting at *H* need not be discussed at this stage. The electron Fermi surface is assumed to be closed, since Shubnikow–de Haas oscillations have been observed for all orientations of **H** with respect to **c** (Soule *et al.* 1964). Near the zone boundary at *H* in figure 28*a*, the cross-section ($\perp$**c**) is circular, but towards the belly

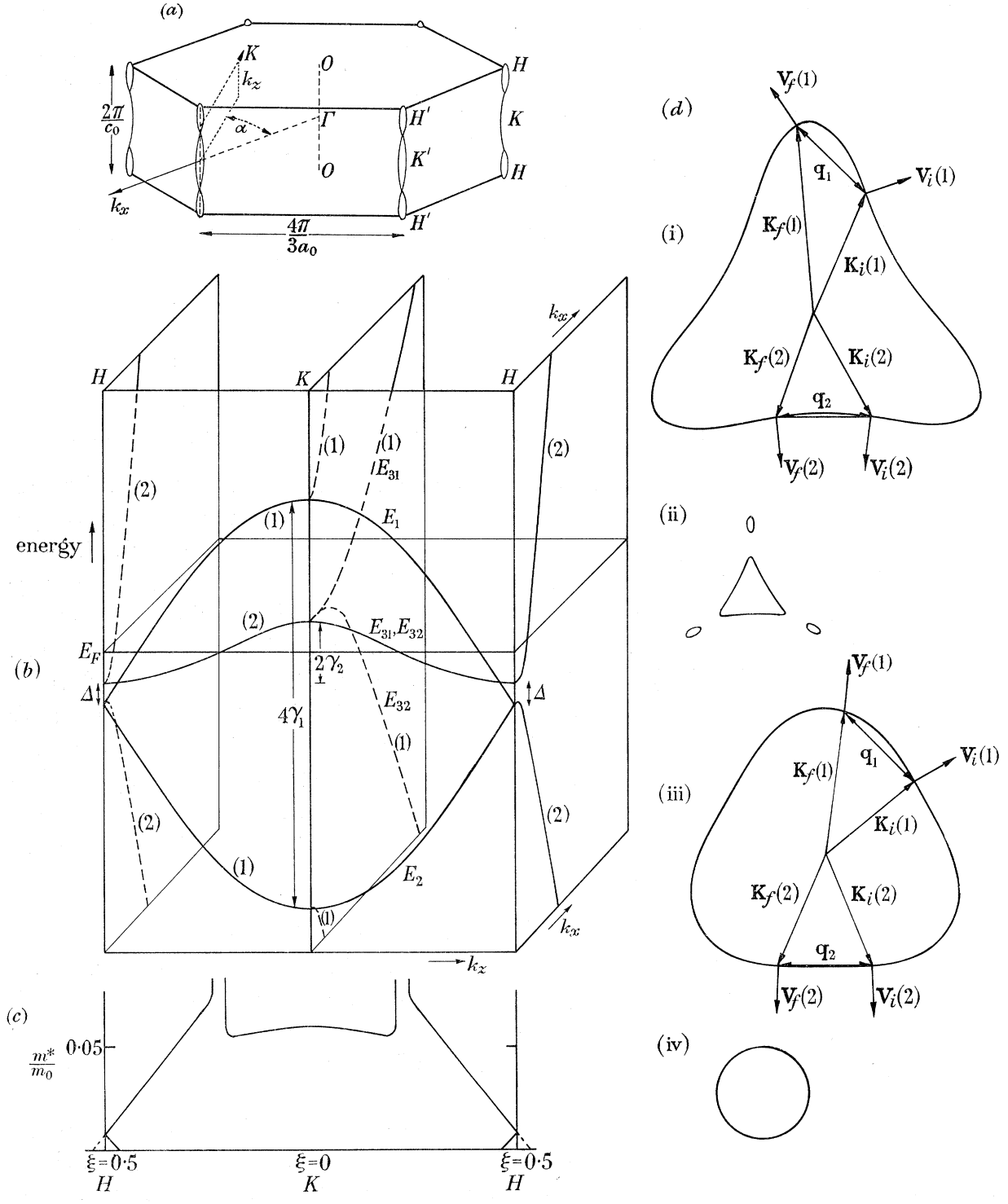

FIGURE 28. For legend see facing page.

the azimuthal radius vector is trigonally modulated in length by about $\pm 10\,\%$ (figure 28*d*). This trigonal warping becomes more pronounced as the high mass extremity remote from the zone edge is approached (where E_3 crosses E_F). For the electron surface the ratio of major to minor axes is about 12·1:1 and the effective mass spectrum, derived from hyperbolic bands, is broad. In general terms the basal plane effective mass is low at the bottom of the band but increases towards the top. This means that apart from the discontinuity at $\xi = 0{\cdot}21$ (figure 28*c*) the effective mass shows a general decrease as one moves along the zone edge from K to H.

On the other hand, the hole Fermi surface, which is also closed, is more strongly trigonally warped at the middle cross-section ($\xi = 0$), yet has a relatively narrow effective mass spectrum. The ratio of major to minor axes is probably nearer 17:1.

For basal plane transport, the most significant portions of the Fermi surface have a large projected area on a cylinder with axis ||**c**. Weighting allowance must be made for differing mobilities of the charge carriers. For descriptive discussion, the middle cross section may be taken as representative of the hole surface ($m_2^* = 0{\cdot}057 m_0$); for electrons we use the corresponding cross section for heavy carriers ($m_1^* = 0{\cdot}039 m_0$) and the extremal ($\pm\pi/c_0$) cross-section for light carriers ($m_3^* \sim 10^{-3} m_0$).

Carriers at the nodes ($\xi = 0{\cdot}21$ in figure 28) are excluded from consideration. They contribute little or nothing to transport because small regions of the Fermi surface are there juxtaposed with high effective masses. This somewhat arbitrary concentration of the carriers into three peaks is a convenient simplification, which has been found quite adequate for the representation of σ_{xx} and σ_{xy} (cf. Soule 1958; McClure 1958).

Inserts to figure 28*d* (i and iii) illustrate the difference between middle cross-sections for electrons and holes respectively. The fact that neither is circular appears to explain many details observed in the present work.

FIGURE 28. Characteristics of the Fermi surface of graphite. (*a*) The Brillouin zone illustrates that the electron and hole surfaces are confined to two sets of non-equivalent vertical edges *HKH* and *H'K'H'* with the coordinate system defined.

(*b*) The variation of energy with reduced wave vector $\xi = k_z c_0/2\pi$ and $\sigma = \frac{1}{2}\sqrt{3} a_0 \kappa$ in the region of a vertical zone edge of the four π bands E_1, E_2, E_{31}, E_{32}. The bands E_{31}, E_{32} are degenerate on the zone edge in the absence of spin orbit splitting. For the energy parameters listed cf. also, McClure (1957, 1964); Dresselhaus & Mavroides (1964). Figure 28 is drawn for $\gamma_3 = 0$, i.e. trigonal warping (Nozières 1958) has not been shown. The numbers (1) and (2) are level degeneracies.

(*c*) Dependence of cyclotron effective mass as a function of $\xi = k_z c_0/2\pi$. In general terms the effective mass decreases as one moves from K to H along the vertical zone edge, the very high effective masses being associated with small areas of the Fermi surface.

(*d*) Typical cross-sections of the Fermi surface in the x–y plane, allowing for trigonal warping ($\gamma_3 \neq 0$). Cross-section (i) represents the belly orbit of the hole surface, i.e. $\xi = 0$; (ii) is typical of a high effective mass region ($\xi = 0{\cdot}21$); (iii) is the belly orbit of the electron surface and (iv) shows that the light electrons ($\xi = 0{\cdot}5$) are planar isotropic and correspond to a relatively small cross section. On surfaces (i) and (iii), two typical $\mathbf{q}_{xy}$ vectors have been superimposed ($\mathbf{q}_1$, $\mathbf{q}_2$) in such a way as to show that the group velocity vector is typically rotated through a larger angle on the hole than on the electron surface. However, such $\mathbf{q}$ vectors would achieve high angle scattering of light electrons ($\xi = 0{\cdot}5$).

PHILOSOPHICAL TRANSACTIONS OF THE ROYAL SOCIETY A MATHEMATICAL, PHYSICAL & ENGINEERING SCIENCES

Analysis of the Hall data in terms of a three-carrier model

Limitations of data arising from the narrow magnetic field range available impose restrictions on the detailed multi-carrier model analysis by the magnetoconductivity tensor method in terms of the two elements (McClure 1958)

$$\sigma_{xx} = \frac{\sigma(H)}{1+(R_H\sigma(H)H)^2} = \sum_{i=1}^{n} \frac{\sigma_{0i}}{1+(H/H_i)^2}, \tag{2·1}$$

$$\sigma_{xy} = R_H\sigma(H)H\sigma_{xx} = \sum_{i=1}^{n} \frac{n_i e_i c(H/H_i^2)}{1+(H/H_i)^2}, \tag{2·2}$$

which are required for an 'isotropic planar' specimen, where the summation extends over the different carriers (i).

Symbols (cf. Beer 1963) have their usual meaning:

$\sigma(H)$	conductivity at field H
R_H	Hall coefficient at field H
σ_{0i}	zero field conductivity attributed to carrier i
n_i	concentration of carrier i; (cm^{-3})
c	velocity of light
H_i	characteristic field for carrier i given by the condiction $\omega_c\,\tau = 1$, i.e.

$$eH_i\tau/m_i^*c = 1; \quad H_i = c/\mu_i.$$

The calculations are conveniently done in the c.g.s. system of units.

Despite the limitations imposed by the range of magnetic fields available, data obtained with SA 26 and SA 20 at 77 °K were sufficiently extensive and reproducible to permit a complete self-consistent calculation of concentrations and mobilities of charge carriers. These calculations used approximately equal concentrations of heavy electrons

$$(m_1^*(\perp\mathbf{c}) = 0{\cdot}039\ m_0)$$

and heavy holes ($m_2^*(\perp\mathbf{c}) = 0{\cdot}057m_0$) together with a much lower concentration of light electrons ($m_3^*(\perp\mathbf{c}) = 1-2\times10^{-3}m_0$) to represent the expected tail towards the light-mass end of the effective mass spectrum for electrons. In order to extract all the quantities required, particularly b ($= \mu_1/\mu_2$), it was necessary to assume that the saturation field, i.e. $H_3 = c/\mu_3$ for carrier 3, was exceeded in the intermediate field region (3000–7000 G) so that

$$(\omega_c\tau)_3 > 1.$$

That this is a reasonable assumption is shown by the experimental plots of R_H against H and particularly by the plots of σ_{xy} against H. Analyses of this type yield a hypothetical (extrapolated) R_0 (2-band) value for the two band ($i = 1, 2$) model, the difference between $R_{0\,(\text{experimental})}$ and $R_{0\,(\text{2-band})}$ being related directly to the zero field Hall coefficient of the light electrons ($i = 3$).

In order to enhance the value of comparisons with Soule's (1958) results, his method of calculation was used. Thus, results of the magnetoconductivity tensor calculations based

on equations (2·1) and (2·2) are illustrated in figure 29 for SA 26 and SA 20 at 77 °K. In this plot, experimental Hall coefficients are compared with the theoretical models detailed in table 6.

Corresponding calculations for the less accurate data illustrated in figure 19 and 20 show the general trends of n_i and μ_i for the three types of carrier, with the additional

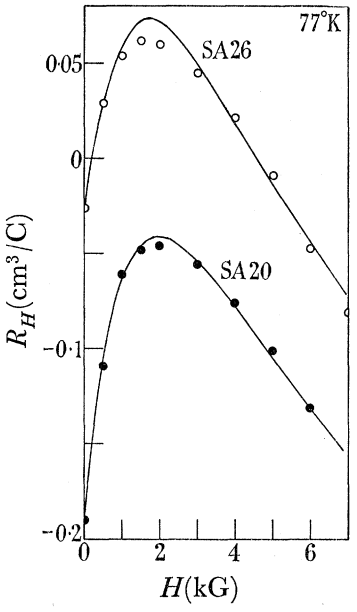

FIGURE 29. Comparison of the experimental values of the basal plane Hall coefficients at 77 °K for SA 26 and SA 20 as a function of field (full lines) with the theoretical values (○ and ●) calculated from the charge carrier concentrations and mobilities listed in table 6.

TABLE 6. CHARGE CARRIER CONCENTRATIONS, MOBILITIES, CHARACTERISTIC FIELDS AND ZERO FIELD PARTIAL CONDUCTIVITIES FOR SA 20 AND SA 26 AT 77 °K ON THE 3-CARRIER MODEL (EQUATIONS (2·1), (2·2))

	i	n_i (cm^{-3})	$10^{-7}\mu_i$ (c.g.s.)	H_i (G)	$10^{-14}\sigma_{0i}$ (c.g.s.)
SA 26	1	$1{\cdot}98\times10^{18}$	1·745	1720	165·5
	2	$1{\cdot}98\times10^{18}$	1·86	1615	176·5
	3	$2{\cdot}44\times10^{16}$	6·4	470	7·4
SA 20	1	$2{\cdot}25\times10^{18}$	1·52	1975	165
	2	$2{\cdot}25\times10^{18}$	1·515	1980	164
	3	$3{\cdot}3\times10^{16}$	6·45	465	10·2
EP 14	1	$2{\cdot}24\times10^{18}$	1·89		calculations due to Soule (1958), McClure (1958) for crystal EP 14 at 77 °K are included for comparison
	2	$2{\cdot}19\times10^{18}$	2·19		
	3*	$3{\cdot}3\times10^{15}$	15		

* At 77 °K this carrier is reported to be a hole. This is a major point of difference between the present results and those of Soule on natural crystals.

finding that on reduction of temperature from 77 °K to 51–53 °K the normal reduction found for n_1 or n_2 is accompanied by an apparent increase in n_3 of about 50 %. The mobility μ_3 exhibits a weaker dependence on temperature in this range than do μ_1, μ_2.

Particularly significant for the present study of trends are the variations with texture of the light electron concentration (n_3).

Characteristics of light electrons (n_3)

Identification of light electrons as carriers derived solely from the second zone counted in the c-axis direction is certainly an over-simplification, but assuming their origin is intrinsic it is correct to link light electrons with the Fermi surface close to points H,H'. Thus, if the concentrations of the heavy carriers are associated with systematic changes of the parameter γ_2 with texture, then the light electrons are strongly linked with Δ (figure 28). For any preparation (e.g. SA 26 or SA 20, table 1), complete analysis of σ_{xx} and σ_{xy} at 77 and 53 °K, shows a regular decrease in concentrations of holes (n_2) and electrons (n_1), much as required by application of Fermi–Dirac statistics to the energy band structure (McClure 1957). Mobilities of the three types of carrier μ_1, μ_2, μ_3 are greater at 53 °K than at 77 °K. But the concentration of light electrons (n_3) actually rises as the temperature falls. With the band model under consideration, this cannot be accounted for simply by adjustment of the Fermi level.

Furthermore, on comparing material SA 20 with the more nearly perfect SA 26 at constant temperature (53 and 77 °K) magneto-conductivity tensor analysis shows that increased imperfections cause an increase in n_3 qualitatively similar to that observed on lowering the temperature, except that the increase associated with defects is accompanied by reduction of all the mobilities μ_i. Passing from SA 20, in which the basal dislocation content is about three orders of magnitude higher, to SA 26, the boundary scattering length changes from about 1 μm to about 2·2 μm.

Two quite different suggestions have been made in the attempt to resolve these apparent inconsistencies about the properties of the light electrons.

(I) The first possibility is that the light carriers primarily arise from charge transfer between the π-electron system, and heteroatomic impurities such as hydrogen or even oxygen. Neglecting any distortion due to impurities, charge transfer to a hole trap at low temperatures cannot account for the experimental findings, since any electron added to the conduction band system would appear at the Fermi surface and would thus not enhance the light electron concentration preferentially. Formation of a simple impurity band, leaving the main band structure undistorted, thus would not suffice to account for the results. To account for the high mobility of the light carriers, the impurity band would need to be broad. If it were far above the Fermi level it would be empty, and if far below it would fill up, in neither case explaining the observed increase in n_3. Simple charge transfer involving impurities thus does not yield a promising explanation.

(II) The second possibility is to accept the main features of the parameterised Slonczewski–Weiss model, and to account for variations in the role of light carriers in terms of variations in actual band structure. Quite generally, the de Haas–van Alphen effect in single crystals and in pyrolytic graphite (Williamson, Foner & Dresselhaus 1965) shows that the band parameter Δ is structure sensitive. In single crystals $\Delta = -25$ meV, whereas it is only -5 meV in pyrolytic graphite. This variation leads to a light electron concentration at helium temperatures of 62×10^{15} cm^{-3} in single crystals and $7{\cdot}5 \times 10^{15}$ cm^{-3} in pyrolytic

graphite. Δ represents the differences in potential energies at the sites of A and A' (or B and B') atoms in the unit cell of graphite. This potential energy is controlled by normal and oblique interactions between layers, and is thus sensitive to variations in interlayer spacing, however caused, as well as to relative displacements of the networks perpendicular to **c**. Interlayer spacing variations can most readily be effected by changes of temperature, or by the application of pressure. Local variations perpendicular to **c** can be readily achieved by basal plane dislocations, or by a flux of longitudinal in-plane phonons.

Effects of texture on details of band characteristics

It is formally convenient to represent the observed effects in terms of an (algebraic) increase of Δ, which in general would increase n_3. Reduction in temperature, which leads to shrinkage of the interlayer separation, or increase in basal plane dislocation content, might of course also affect the electrical properties in other ways. Effects not included might contribute considerable terms; allowance may be needed for spin-orbit splitting at the hexagonal face, which like Δ appears to be structure sensitive (Williamson *et al.* 1965). Furthermore, it must be an over-simplification to assume that hexagonal symmetry is preserved in the strain fields of dislocations and to attribute their effects solely to variation in spacing of the levels. Thus the low stacking fault energy in graphite leads to dissociation into partial dislocations separated by a region of rhombohedral symmetry. Allowance for such textural effects on the band structure would be tantamount to incorporating a local symmetry change in a deformation potential parameter which would raise the degeneracy of E_3 along HKH (figure 28). Up to the present, no wholly rhombohedral well oriented graphite has been produced experimentally, nor is the band model for such a substance fully described. Because of such perturbations, pyrolytic graphite in which the basal plane exhibits a microcrystalline texture even after hot pressing and annealing, may show fine differences from ideal single crystal graphite. In the light of the preceding discussion, some further refinements can be made even to a two-carrier model.

The mobility ratio $b = \mu_1/\mu_2$

The T_1 magnetoresistance at 3 kG, where the two-carrier model is a good approximation, yields significant values of the mean mobility $\bar{\mu} = (\mu_1\mu_2)^{\frac{1}{2}}$ provided the temperature T is sufficiently high so that σ_{01} and σ_{02} are both much larger than σ_{03}. The magnetic field must also lie below the onset of any saturation effects for the two majority carriers ($i = 1, 2$). With these limitations, $\bar{\mu}$ is a function of temperature increasing regularly to limiting values as the crystallite size is increased and the basal plane dislocation concentration is reduced. This analysis thus confirms the overall boundary scattering length derived from thermal conductivity, but does not reveal details of electron and hole scattering.

With the two-carrier model, b varies systematically with temperature, and also with sample perfection, as calculated from Hall data. Some differences are found from single crystal results (EP 14, Soule 1958).

For all specimens, at high temperatures, b is about 1·1. It decreases as the temperature falls (figure 21) and depends more sensitively on imperfection content. With the best

graphites of the present series, the ratio b passes through a minimum, rising again towards unity at about 55 °K. A minimum is also found with the less perfect samples, but b remains above unity throughout. The initial fall is considered to be intrinsic for all samples, since it occurs in a range of temperatures dominated by phonon scattering. The subsequent rise in b at lower temperatures is clearly enhanced as the dislocation content increases. This effect appears to be associated with their presence.

Phonon-charge carrier interactions

Interpretation of the two trends discussed above in full detail requires precise knowledge of the Fermi surface, as well as of the interactions between phonons and both types of charge carrier. A simplified model can serve to identify the main features (cf. Sugihara & Sato (1963) except that γ_3, the trigonal warping parameter (1955, 1956) is here assumed zero). Two phonon modes are important:

(i) For in-plane longitudinal vibrations, the characteristic temperature is high

$$(\theta = 1400\ ^\circ\mathrm{K}).$$

At low values ($< 0{\cdot}2$) of T/θ the dispersion curve in the q_x, q_y plane is linear (Yoshimori & Kitano 1956). Assuming the shear modulus C_{44} is small, the surfaces of constant frequency in reciprocal space are then cylinders with axis parallel to the c axis centred on the point Γ. Phonons in this group will accordingly scatter electrons through progressively smaller angles as the temperature falls, but will not influence c-axis transport.

(ii) Out-of-plane vibrations for which the characteristic temperature is a function of the direction of propagation: with the consequence that surfaces of constant frequency are complicated (Yoshimori & Kitano 1956). Parallel to the c axis, the estimated characteristic temperature for the longitudinal acoustic mode is $\theta = 185$ °K (Dolling & Brockhouse 1962); in the direction of the basal plane θ may be as high as 1000 °K. As the temperature of the specimen is raised from 0 °K, as a consequence of this steep angular dependence, surfaces of constant (reduced) frequency ν/ν_D expand proportionately much more rapidly along the c axis than along the a axis. (ν_D is the limiting frequency $k\theta/h$ in each direction). These surfaces first touch the centre (O) of the hexagonal zone face. Off-axis phonons of this mode will be able to scatter charge carriers through high angles, first with respect to c-axis conduction and then at higher temperatures also with respect to basal plane conduction. A further peculiarity is that parallel to the c axis, intervalley electron-hole scattering will become possible.

Higher values of b which are observed on lowering the temperature or on passing to less perfect samples at constant temperature, can be interpreted on the basis of trigonally warped Fermi surfaces ($\gamma_3 \neq 0$) in terms of the bias imposed on low-angle scattering. In any low-angle scattering event occurring in the basal plane, the propagation vector $\mathbf{k}_i$ is rotated by $\Delta\mathbf{q}$ to a new value $\mathbf{k}_f$ such that $\mathbf{k}_i - \mathbf{k}_f = \pm\Delta\mathbf{q}$ with $\mathbf{k}_i, \mathbf{k}_f > \Delta\mathbf{q}$. The group velocity vector will not in general rotate through the same angle. In particular, when $\mathbf{k}_i$ and $\mathbf{k}_f$ lie in a region of high curvature, the group velocity vector will be rotated through a higher angle, than if the curvature is low. As illustrated in figure 28, the average curvature

to be expected at the maximum cross section is larger in the case of holes than for electrons.† Qualitatively, low-angle scattering should reduce hole mobility more than that of the electrons.

Even with this simplified model, direct calculations of b are not feasible in the absence of knowledge of $\tau_i(\alpha)$. The general trend as the vector $\Delta\mathbf{q}$ increases can be inferred, since $\bar{\beta}$ tends towards $1/r_0$ and thus the ratio $\bar{\beta}(\text{holes})/\bar{\beta}$ (electrons) tends towards unity. This implies isotropic scattering with $b \to 1$ as the scattering angle increases.

According to this interpretation, as the temperature is reduced low angle scattering will increasingly predominate, being in turn overtaken by boundary scattering as the dominant term. Boundary scattering becoming generally effective is consistent with the small cross section area of the Fermi surface. Observed correlations with sample perfection and temperature follow, if basal plane dislocations scatter through low angles, similarly to in-plane longitudinal phonons. It would also follow that the deformation potential of such basal plane dislocations must be very small. This would agree with their apparent failure to affect the mean mobility $\bar{\mu}$. Because of the lower cross section area near H,H', high angle scattering of light carriers will remain dominant to low temperatures.

Thermoelectric power

In the temperature range 50 to 250 °K the thermoelectric power becomes progressively more negative as the specimens contain more imperfections (figure 23). It seems unlikely that this correlation is accounted for by trends in phonon drag, since scattering at crystallite boundaries rather than by phonons appears to determine both phonon and electron path lengths at the lower end of the temperature range. Furthermore, even if the electron-phonon interaction were strong enough for phonon drag to be a powerful influence, the separate effects on the electron and hole surfaces should be nearly self-cancelling (Mills, Morant & Wright 1965; Goldsmid & Lacklison (1965) found no evidence for phonon drag.)

Neglecting phonon drag altogether, the behaviour to be expected may conveniently be calculated from a two-band model (cf. Klein 1964) from thermoelectric data. The ratio b_s $(= \mu_1/\mu_2)$ is found from the expression which applies to the so-called standard two-band model.

$$S_a = \frac{k}{e}\left(\frac{1-b_s}{1+b_s}\right)\left\{\frac{2F_i(E_0/2kT)}{F_0(E_0/2kT)} - \frac{E_0}{2kT}\right\}, \tag{3}$$

in which F_i, F_0 are tabulated Fermi integrals and the band overlap is taken as 0·01 eV in conformity with experimental values of S_a at room temperature. Present results show that

† Quantitatively, if the section of the electron surface for the sake of example is represented by

$$r_\alpha = r_0(1+0{\cdot}1\cos 3\alpha)$$

and the hole surface by $r_\alpha = r_0(1+0{\cdot}2\cos 3\alpha)$ calculation of the average curvature from the conventional expression

$$\bar{\beta} = \frac{\int_0^{60} \beta_\alpha \left[r_\alpha\left(1+\frac{1}{r^2}\frac{\mathrm{d}\alpha}{\mathrm{d}r}\right)\right]^{\frac{1}{2}} \mathrm{d}\alpha}{\int_0^{60}\left[r_\alpha\left(1+\frac{1}{r^2}\frac{\mathrm{d}\alpha}{\mathrm{d}r}\right)\right]^{\frac{1}{2}}\mathrm{d}\alpha},$$

$$r_\alpha = r_0(1+0{\cdot}1\cos 3\alpha),$$

and

$$r_\alpha = r_0(1+0{\cdot}2\cos 3\alpha),$$

where β_α is the curvature at angle α, yields a ratio $\bar{\beta}(\text{holes})/\bar{\beta}(\text{electrons})$ of 1·36 which illustrates the view put forward.

at lower temperatures the correction for the role of the light electrons ($i = 3$) becomes unavoidable, modifying the two carrier expression (3). A tentative correction to b_H, the ratio μ_1/μ_2 calculated from the 2-carrier model applied to the Hall effect, referred to above, allows for the increasing importance of the term σ_{03} as the temperature is lowered, or the content of imperfections is raised. A weighted ratio b^* is defined by

$$b^* = \frac{n_1\mu_1 + n_3\mu_3}{n_2\mu_2}.$$

Both μ_1/μ_2, and the parameters n_3 and μ_3 increase as the temperature falls below 77 °K, and b^* must increase more rapidly than does b_H. Values of b^* evaluated in this way follow the apparent trend of b_s more closely than does b_H (cf. table 7). The large negative thermoelectric power below 77 °K is thus attributed to the role of light electrons in these materials.

TABLE 7. COMPARISONS OF MOBILITY PARAMETERS IN RELATION TO TEXTURE

	SA 26			SA 20 (assumed equivalent to SA 24)		
	53 °K	77 °K	300 °K	53 °K	77 °K	300 °K
b_H	0·970	0·946	1·09	1·041	0·992	1·11
b_s	1·14	1·05	1·08	1·16–1·18	1·12	1·08
b^*	1·13	1·05	1·09	1·17	1·13	1·11

The properties of ideal graphite

Unavoidably, even three-carrier models with various degrees of sophistication give only approximate representations of the spectrum of carrier masses in graphite, and of their mobilities. Even so, parameters derived from the experimental data by their means provide useful numerical quantities for the correlation of trends associated with crystal defects. As already stressed, the range of textures now studied lies much closer to ideal graphite, and is much less extensive, than in previous discussions on carbons and graphites of varying perfection (Blackman *et al.* 1961).

Trends now established substantiate the view that many of the numerical data reported for basal plane properties for the 'best' crystal of natural graphite (EP 14, Soule 1958), may be taken as close to the asymptotic limit for defect-free graphite. This applies, for example, to the mean mobility $\bar{\mu}$ on a two-band model (figure 6), to the resistivity/temperature plot (figure 4) and to values of the Hall coefficient at room temperatures and high fields (figure 18). On the other hand, for conditions where light electrons affect the overall electronic properties appreciably (e.g. figure 19, figure 20), the best natural crystals do not appear to provide a reliable norm. Indeed the appearance of 'light holes' in natural crystals as reported by Soule (1958) is not consistent at all with the presently accepted band model.

The temperature dependence of c-axis resistivity presents unsolved theoretical problems. If, as argued above, disturbing effects due to path tortuosity can properly be neglected, then above 60 °K the mean free path in the c-axis direction is estimated to be of the order of one or two lattice spacings. On the conventional view, the Fermi contraction as the temperature falls could explain the observed initial rise in resistance in terms of a decrease in number of carriers. Experiment now shows that on cooling below 60 °K the temperature

coefficient of resistivity falls to zero and eventually becomes positive. So far as is known the Fermi contraction is monotonic with further reduction of temperature. The mean free path λ_c must thus rise as one cools below 60 °K. Such a rise is in fact necessary to account for Shubnikow–de Haas oscillations and cyclotron resonance around 4 °K with $\mathbf{H} \perp \mathbf{c}$. Observations of such effects provide an overriding criterion for a lengthened mean free path in the c-axis direction at 4·2 °K.

It remains to be verified whether existing band models can ever satisfactorily account for c-axis properties above 60 °K.

Thanks are due by one of us (I.S.) to the Central Electricity Generating Board for a research stipend.

References

Ammar, A. & Young, D. A. 1964 *Br. J. Appl. Phys.* **15**, 131.

Bate, R. T. & Beer, A. C. 1961 *J. Appl. Phys.* **32**, 800.

Beer, A. C. 1963 Galvanomagnetic effects in semiconductors in *Solid state physics*, Suppl. 4 (Eds Seitz & Turnbull). Academic Press.

Blackman, L. C. F., Saunders, G. A. & Ubbelohde, A. R. 1961 *Proc. Roy. Soc.* A **264**, 19.

Dolling, G. & Brockhouse, B. N. 1962 *Phys. Rev.* **128**, 1120.

Drabble, J. R. & Wolfe, R. 1956 *Proc. Phys. Soc.* (*Lond.*) B**69**, 1101.

Dresselhaus, M. S. & Mavroides, J. G. 1964 *I.B.M. J. Res. Dev.* **8**, 262.

Frederikse, H. P. R. & Hosler, W. R. 1957 *Phys. Rev.* **108**, 1136.

Gerlach, E. 1962 *Z. Phys.* **166**, 81. See also Langbein, D. 1962 *Z. Phys.* **166**, 22.

Goldsmid, H. J. & Lacklison, D. E. 1965 *Brit. J. Appl. Phys.* **16**, 573.

Hennig, G. R. & Hove, J. E. 1956 *Proc. Int. Conf. on the Peaceful Use of Atomic Energy* **7**, 666.

Hooker, C. N., Ubbelohde, A. R. & Young, D. A. 1963 *Proc. Roy. Soc.* A **276**, 83.

Hooker, C. N., Ubbelohde, A. R. & Young, D. A. 1965*a* *Proc. Roy. Soc.* A **284**, 17.

Hooker, C. N., Ubbelohde, A. R. & Young, D. A. 1965*b* *Second Conference on industrial carbon and graphite, London*: Society of Chemical Industry.

Isenberg, I., Russell, B. R. & Greene, R. F. 1948 *Rev. Sci. Instrum* **19**, 685.

Jan, J–P. 1957 *Solid state physics* (Eds Seitz & Turnbull), **5**, 1. New York: Academic Press.

Johnston, D. F. 1955 *Proc. Roy. Soc.* A **227**, 349.

Johnston, D. F. 1956 *Proc. Roy. Soc.* A **237**, 48.

Kinchin, G. H. 1953 *Proc. Roy. Soc.* A **217**, 9.

Klein, C. A. 1964 *J. Appl. Phys.* **35**, 2947.

Klein, C. A., Straub, W. D. & Diefendorf, R. J. 1962 *Phys. Rev.* **125**, 468.

McClure, J. W. 1957 *Phys. Rev.* **108**, 612.

McClure, J. W. 1958 *Phys. Rev.* **112**, 715.

McClure, J. W. 1964 *I.B.M. J. Res. Dev.* **8**, 255.

McClure, J. W. & Smith, L. B. 1961 *Proc. 5th Carbon Conference*, vol. 2, p. 3. Oxford: Pergamon.

Mills, J. J., Morant, R. A. & Wright, D. A. 1965 *Br. J. Appl. Phys.* **16**, 479.

Moore, A. W., Ubbelohde, A. R. & Young, D. A. 1964 *Proc. Roy. Soc.* A **280**, 153.

Nozières, P. 1958 *Phys. Rev.* **109**, 1510.

Nye, J. F. 1957 *Physical properties of crystals*. Oxford University Press.

Olsen, G. H. 1962 *Wireless World* **68**, 56.

Primak, W. & Fuchs, L. H. 1954 *Phys. Rev.* **95**, 22.

Putley, E. H. 1960 *Hall effect and related phenomena*. London: Butterworths.

Slonczewski, J. C. & Weiss, P. R. 1958 *Phys. Rev.* **109**, 272.

Soule, D. E. 1958 *Phys. Rev.* **112**, 698.

Soule, D. E., McClure, J. W. & Smith, L. B. 1964 *Phys. Rev.* **134** A, 453.

PHILOSOPHICAL TRANSACTIONS OF THE ROYAL SOCIETY A MATHEMATICAL, PHYSICAL & ENGINEERING SCIENCES

Spain, I. L., Ubbelohde, A. R. & Young, D. A. 1965 *Second conference on industrial carbon and graphite.* London: Society of Chemical Industry.
Sugihara, K. & Sato, H. 1963 *J. Phys. Soc. Japan* **18**, 332.
Ubbelohde, A. R., Young, D. A. & Moore, A. W. 1963 *Nature, Lond.* **198**, 1192.
Williamson, S. J., Foner, S. & Dresselhaus, M. S. 1965 *Phys. Rev.* **140** A, 1429.
Wyckoff, R. W. G. 1960 *Crystal structures*, vol. 1. (Interscience.)
Yoshimori, A. & Kitano, Y. 1956 *J. Phys. Soc. Japan* **11**, 352.

PHILOSOPHICAL TRANSACTIONS OF THE ROYAL SOCIETY A MATHEMATICAL, PHYSICAL & ENGINEERING SCIENCES

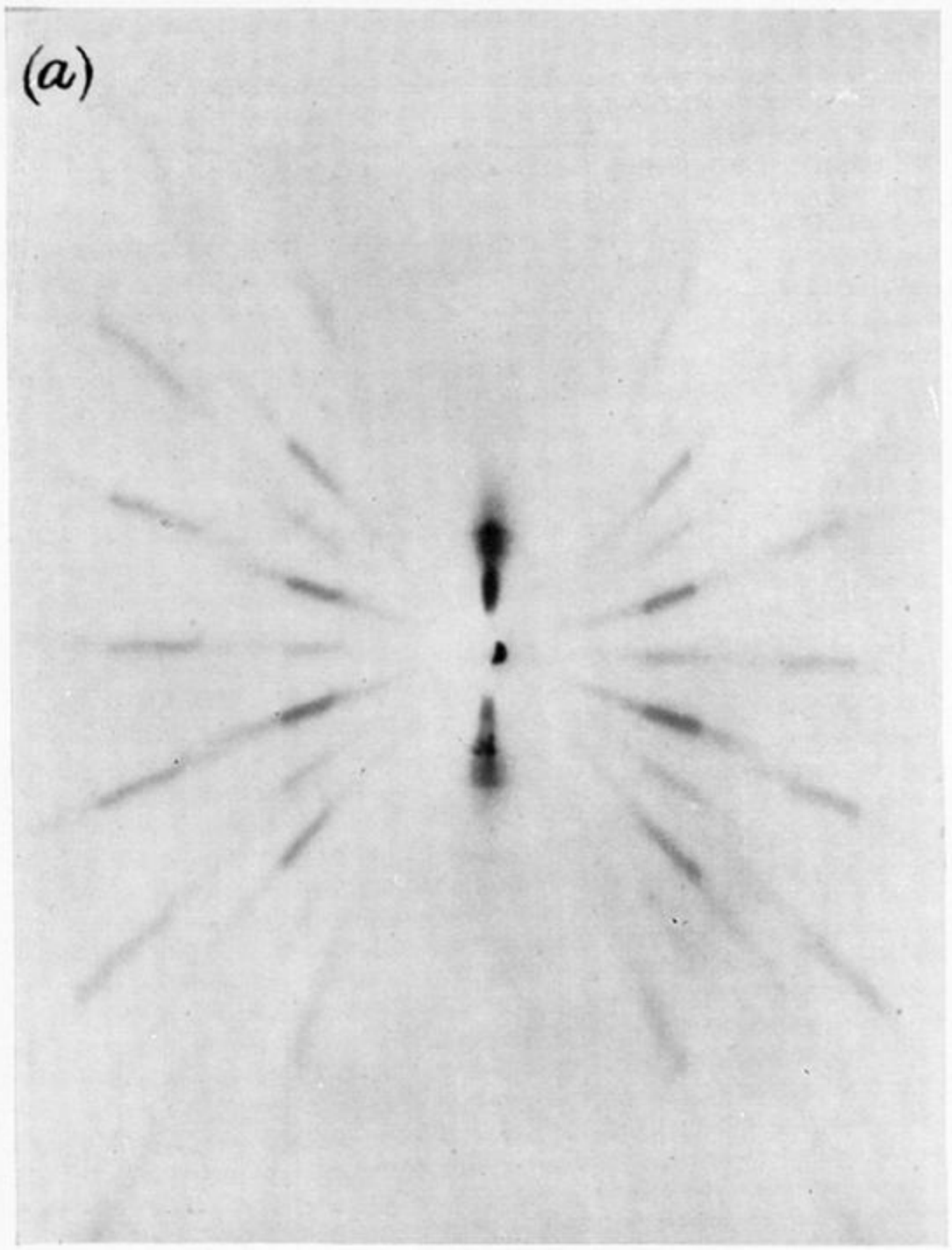

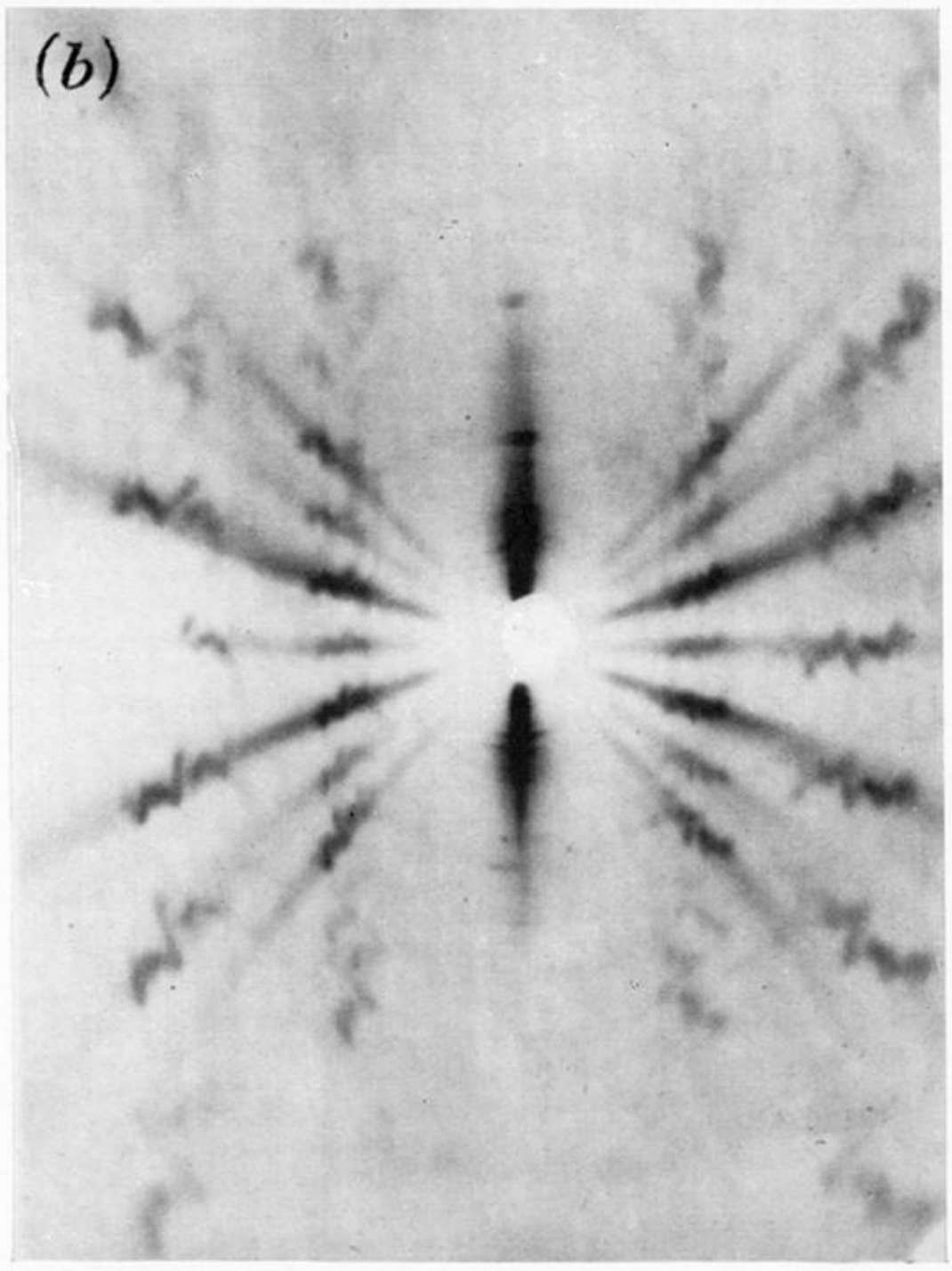

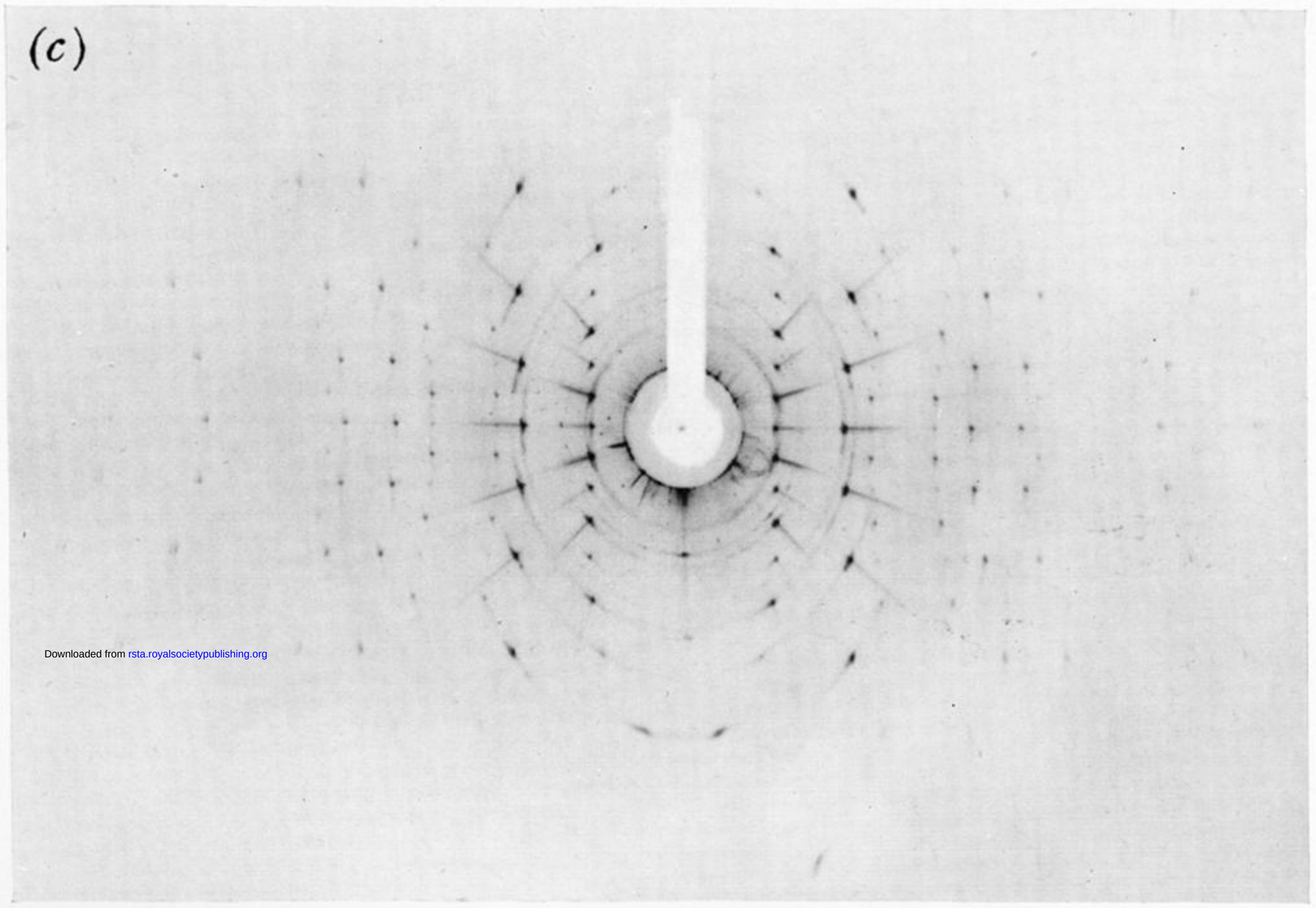

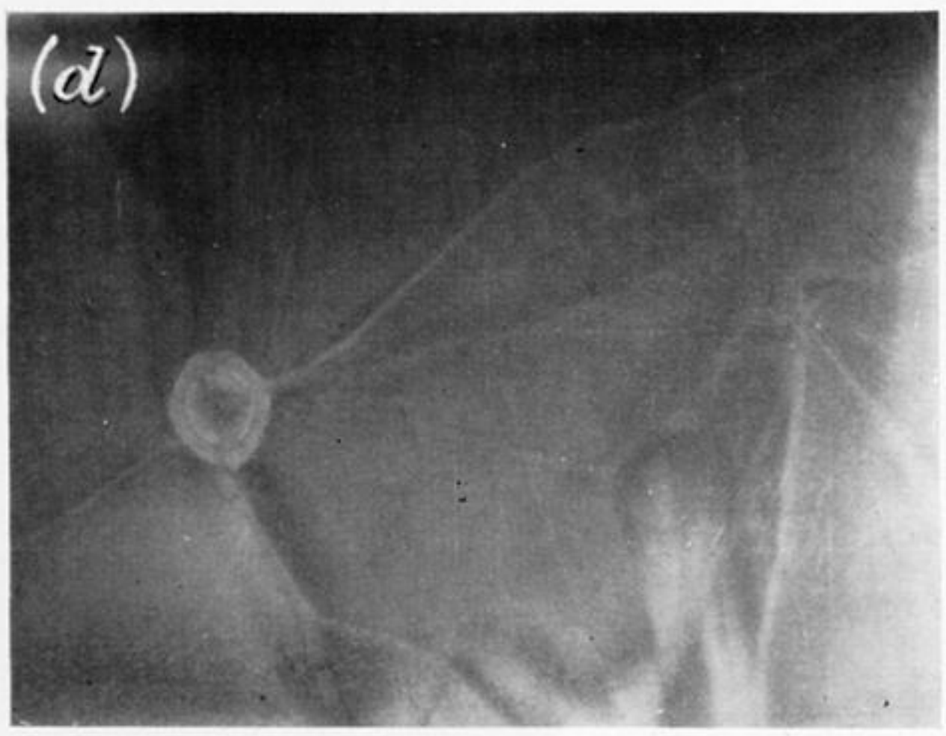

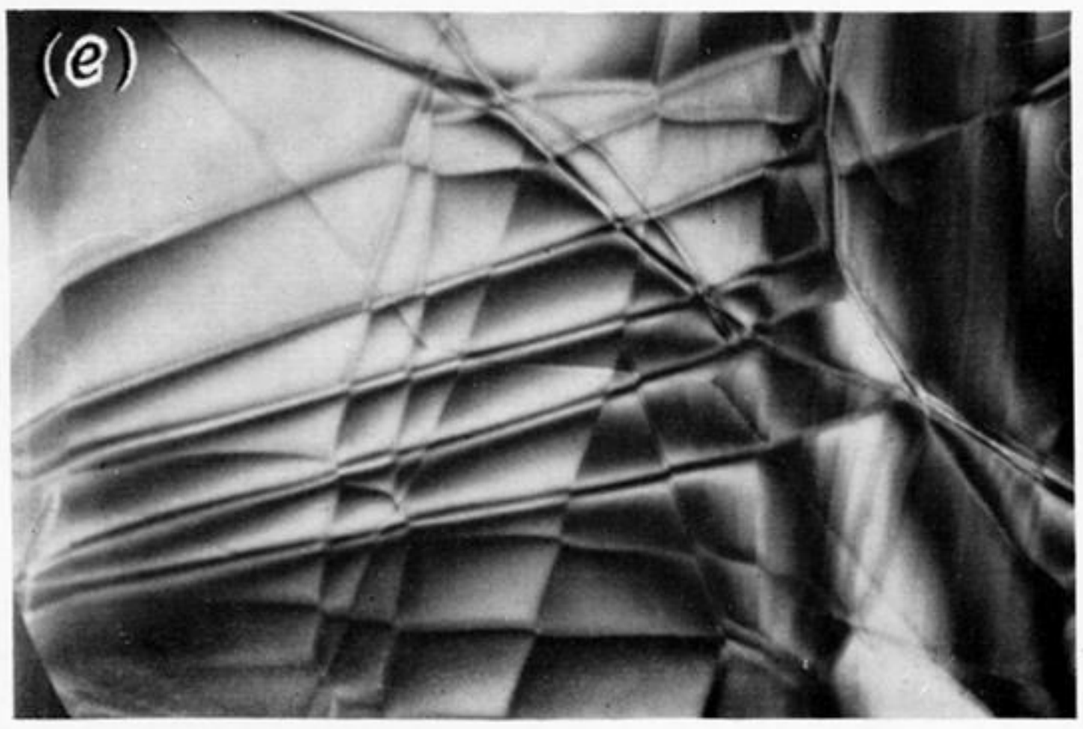

FIGURE 1. (*a*) X-ray photograph of flat disk (IFP 53) taken with Mo$K\alpha$ beam parallel to basal planes. Note isostatic zone at the edge of the disk. (Moore *et al.* 1964; Spain *et al.* 1965). (*b*) As above, but for a rippled cleavage surface (Sample IFP 1). (*c*) X-ray diffraction pattern (Mo$K\alpha$) of sample SA 26 (JHP 1) taken on a cylindrical film. Note $\alpha_1\,\alpha_2$ splitting. (*d*) Electron micrograph of a soot nucleus (magn. $\times 6500$) (IFP 37) (Moore *et al.* 1964). (*e*) Basal dislocation network in annealed material (magn. $\times 6500$) (IFP 37).